# Evaluation of a Fused Sonomyography and Electromyography-Based Control on a Cable-Driven Ankle Exoskeleton

Qiang Zhang , Member, IEEE, Krysten Lambeth , Graduate Student Member, IEEE, Ziyue Sun, Albert Dodson, Xuefeng Bao, Member, IEEE, and Nitin Sharma, Senior Member, IEEE

Abstract—This article presents an assist-as-needed (AAN) control framework for exoskeleton assistance based on human volitional effort prediction via a Hill-type neuromuscular model. A sequential processing algorithm-based multirate observer is applied to continuously estimate muscle activation levels by fusing surface electromyography (sEMG) and ultrasound (US) echogenicity signals from the ankle muscles. An adaptive impedance controller manipulates the exoskeleton's impedance for a more natural behavior by following a desired intrinsic impedance model. Two neural networks provide robustness to uncertainties in the overall ankle joint-exoskeleton model and the prediction error in the volitional ankle joint torque. A rigorous Lyapunov-based stability analysis proves that the AAN control framework achieves uniformly ultimately bounded tracking for the overall system. Experimental studies on five participants with no neurological disabilities walking on a treadmill validate the effectiveness of the designed ankle exoskeleton and the proposed AAN approach. Results illustrate that the AAN control approach with fused sEMG and US echogenicity signals maintained a higher human volitional effort prediction accuracy, less ankle joint trajectory tracking error, and less robotic assistance torque than the AAN approach with the sEMG-based volitional effort prediction alone. The findings support our hypotheses that the proposed controller increases human motion intent prediction accuracy, improves the exoskeleton's control performance, and boosts voluntary participation from human subjects. The new framework potentially paves a foundation for using multimodal biological signals to control rehabilitative or assistive robots.

Manuscript received 1 September 2022; revised 23 November 2022; accepted 3 January 2023. Date of publication 9 February 2023; date of current version 7 June 2023. This paper was recommended for publication by Associate Editor S. Crea and Editor E. Yoshida upon evaluation of the reviewers' comments. This work was supported by the National Science Foundation CAREER Award under Grant 2002261. (Corresponding author: Nitin Sharma.)

This work involved human subjects or animals in its research. Approval of all ethical and experimental procedures and protocols was granted by the Institutional Review Board of North Carolina State University under Application No. 20602, and performed in line with the guidelines of the Declaration of Helsinki.

Qiang Zhang, Krysten Lambeth, Albert Dodson, and Nitin Sharma are with the Joint Department of Biomedical Engineering, University of North Carolina at Chapel Hill and North Carolina State University, Raleigh, NC 27695 USA (e-mail: qzhang25@ncsu.edu; kflambet@ncsu.edu; aedodson@ncsu.edu; nsharm23@ncsu.edu).

Ziyue Sun is with DiDi Labs, Mountain View, CA 94043 USA (e-mail: sunziyue01@gmail.com).

Xuefeng Bao is with the Department of Biomedical Engineering, University of Wisconsin-Milwaukee, Milwaukee, WI 53221 USA (e-mail: baox@uwm.edu).

This article has supplementary material provided by the authors and color versions of one or more figures available at https://doi.org/10.1109/TRO.2023.3236958.

Digital Object Identifier 10.1109/TRO.2023.3236958

Index Terms—Ankle exoskeleton, assist-as-needed (AAN) neuromuscular model, sonomyography, control. surface electromyography (sEMG), ultrasound (US) imaging.

# Nomenclature

AAN	Assist-as-needed.

**HNM** Hill-type neuromuscular model. Surface electromyography. **sEMG** 

**EMG** Electromyography. US

Ultrasound.

AIC Adaptive impedance controller.

NN Neural network. ID Inverse dynamics. **CNS** Central nervous system. **HMI** Human-machine-interface.

**RBFNN** Radial basis function neural network.

**SNR** Signal-to-noise ratio.

BCD-AnkleExo Bidirectional cable-driven ankle exoskeleton.

**GAS** Gastrocnemius. LGS Lateral gastrocnemius.

SOL Soleus.

MTU Muscle-tendon-unit.

CE Contractile element. PE Passive element. RHS Right-hand side.

**SEA** Series-elastic actuator. **RMSE** Root mean square error. **IRB** Institutional Review Board.

S1Scenario 1. **S**2 Scenario 2. S3 Scenario 3.

SD Standard deviation. **GRF** Ground reaction force. B-mode Brightness mode. **ANOVA** Analysis of variance.

Tukey's HSD Tukey's honestly significant difference test. **GAPSO** Genetic algorithm-based particle swarm op-

timization.

#### I. INTRODUCTION

OCOMOTION accounts for a dominant part of human activities in daily living, such as moving around the

1552-3098 © 2023 IEEE. Personal use is permitted, but republication/redistribution requires IEEE permission. See https://www.ieee.org/publications/rights/index.html for more information.

community, going to work or school, doing errands, etc. The human ankle plantarflexors play an essential role in achieving locomotion, especially for generating a large burst of "push-off" mechanical power during the late stance phase that enables the forward and upward acceleration of the center of mass. However, a variety of neurological disorders, such as spinal cord injury, stroke, and multiple sclerosis, weaken the plantarflexion function, cause a dramatic decrease in the "push-off" power that impairs walking, leading to a poor energy economy [1], and disrupt both physical and emotional well-being [2].

Recent advanced robotic devices, such as powered ankle exoskeletons [3], [4], [5], [6], ankle emulators [7], [8], soft exosuits [9], [10], and hybrid neuroprostheses [11], [12], [13], [14], [15], either aim to help people with neurological disorders regain ankle joint mobility and improve gait patterns or augment limb function and improve the energy economy in persons without disabilities. Controllers in these robotic devices predominantly provide a priori defined torque/angle profiles [7], [10], [16], [17], [18], while some use neuromuscular reflexive rules [5], [19] that are event-triggered during different gait phases. The predefined joint torque profiles have also been optimized via human-in-the-loop optimization methods to reduce metabolic cost [7], [16] or muscles' EMG/sEMG activities [19]. However, these control approaches mainly emphasize human augmentation and may not be designed to encourage human volitional effort, a relevant objective for neurorehabilitation.

A user-driven assistive device control approach can arguably improve walking performance in people with neurological disorders [20], [21], [22]. Considering human motion intent/voluntary effort while computing minimal robotic assistance, also known as AAN control, is essential to increase muscle activities of the subject, encourage neuroplasticity, and maximize the recovery effects during rehabilitation training [23], [24], [25]. Wolbrecht et al. [23] developed a model-based adaptive AAN approach to learn the patient's abilities and assist in completing movements while remaining compliant. Hussain et al. [24] proposed an AAN control architecture for providing seamless adaptive robotic assistance to hip and knee joints during gait training, powered by pneumatic muscle actuators. Asl et al. [25] proposed a novel adaptive NN controller with input saturation to address the unknown system dynamics and external disturbances on the hip and knee joints of a lower limb robotic exoskeleton. These studies used NNs to estimate human volitional effort, which depended on the measures of interaction dynamics or estimates of the joint torque from ID. However, the nature of interaction dynamics and ID may not be appropriate in some cases, as the users must produce a torque on the joints that exceeds some threshold to initiate the motion before the devices can generate assistance. For example, if the users have high-level muscle weakness and are not able to produce sufficient torques on their joints, such as may be the case of individuals with severe impairments, the robotic devices may not be successfully controlled. Fortunately, this disadvantage can be avoided by using the human intent-based control of robotic devices according to physiological signals, like sEMG, that are sent from the CNS to the functional motor units.

Computing appropriate robotic assistance in an AAN control approach may be accomplished by predicting the user-generated

volitional effort or motion intent from skeletal muscles' sEMG signals. In recent years, the use of sEMG-driven HNMs, as a HMI to estimate the motion intent or residual volitional effort, has been particularly motivated to implement bio-inspired AAN control for enhancing the voluntary participation of the user. For example, myoelectric controllers [19], [26], [27], [28] proportionally assist the user based on real-time recorded EMG signals. However, these model-free methods directly relied on sEMG signals and disregarded the highly nonlinear transformation from sEMG onset to joint torque generation. Instead, the neuromuscular model-based AAN control methods [29], [30], [31], [32] use a nonlinear mapping to predict limb torques from sEMG signals. Subsequently, the proportional adjustment of the robotic assistance according to the biological joint torque estimation could be achieved [30], [31], [32]. Some studies bypassed the use of the complex neuromuscular model [33], [34] in the AAN control. Instead, the rectified and low-pass filtered EMG signals were used as inputs to a RBFNN that was incorporated into a Slotine-Li adaptive controller [35].

Despite sEMG's impressive performance and wide application in rehabilitative/assistive device control, its susceptibility to signal interference coming from neighboring muscles, low SNR, and inability to measure contractions of deeply located muscles [36], [37], [38] are significant hurdles for sEMG's use in HMIs and accurate muscle activation measures. As an alternative to sEMG-based HMIs, US imaging has recently been applied to quantitatively measure muscle contractility. Its advantages over sEMG include direct muscle visualization, high SNR, and access to deep muscle layers. One-dimensional (pennation angle, fascicle length, muscle thickness [39], and echogenicity/image intensity [38], [40], [41], [42]), two-dimensional (tissue displacement or strain [43], [44]), and high-dimensional (implicit features from deep learning [45]) features have been investigated to characterize the muscle contraction force, net joint torque, and joint movement. However, nearly all studies above were offline due to computationally intensive US imaging beamforming and postprocessing. In a recent study [46], the SOL muscle average velocity profiles during versatile walking tasks were measured through prerecorded US images and then used to estimate the muscle force and determine the exosuit assistance profile, which was proportional to the estimated muscle force. The musclebased assistance approach was evaluated by calculating the reduction of metabolic cost with a bilateral ankle exosuit in a variety of walking conditions. Although this muscle-based approach enables a rapid generation of individualized assistance profiles, the US images were processed offline; thus, the realtime feedback from US imaging-derived signals that estimate muscle force remains unexplored. Importantly, given the timevarying nature of the muscle force generation among gait cycles and the highly nonlinear relationship between muscle contractility and muscle force/joint moment, the desired assistance may deteriorate in the absence of real-time US imaging-derived feedback.

Considering the aforementioned corresponding advantages of both sEMG- and US imaging-based HMIs, recent evidence from offline studies has shown that the joint torque or motion intent prediction accuracy can be further increased by fusing US imaging-derived and sEMG-derived measures of muscle

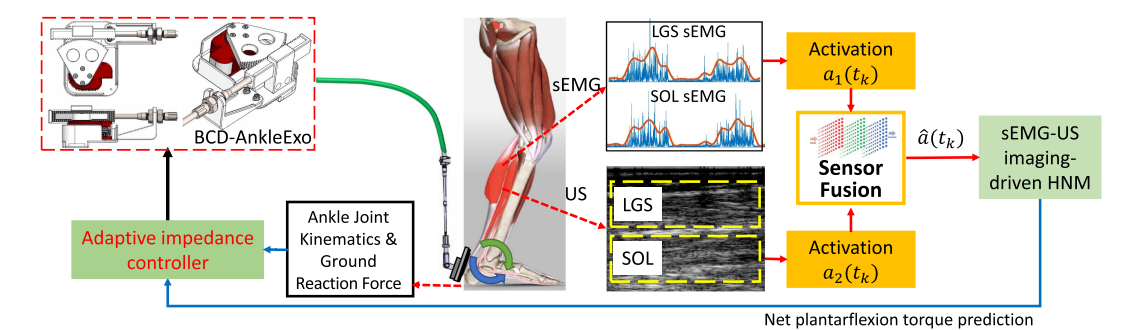


Fig. 1. Overview of the voluntary torque prediction via the sEMG-US imaging-driven HNM that incorporates an AIC for adjusting the assistance of a novel BCD-AnkleExo.

contractility [37], [47], [48], [49]. A probable reason for the improved accuracy of the dual-modal approach is that the dualmodal signals provide complementary electrical and mechanical information regarding the same muscle contraction activity. From the perspective of human volitional effort or motion intent prediction, since there is a lack of real-time methods for fusing sEMG and the US-derived signals, motivation exists to develop a data fusion algorithm for predicting the joint torque or motion intent online. Furthermore, few AAN control studies for robotic assistive devices have focused on the ankle joint or used any real-time sensor fusion between sEMG and US imaging signals, especially for locomotion tasks, to the best of the authors' knowledge. Therefore, there is also a need for incorporating the novel data fusion algorithm into the control design of wearable robotic assistive devices, thus promoting a greater symbiosis between the robotic assistive device and the user.

To tackle these motivations, there are two main challenges: 1) the sparsity of US imaging measurement feedback, which causes different sampling rates of the US imaging and sEMG signals when used in the real-time closed-loop control framework; and 2) the design of an intuitive AAN controller to adapt to the time-varying residual volitional effort or motion intent from HMIs. In this article, for the first time, we propose to combine US imaging—derived echogenicity signals with sEMG signals to continuously predict human ankle joint net plantarflexion torque online during a walking task. The AAN control design incorporates the volitional effort prediction and an AIC to automatically adjust the assistance levels from a BCD-AnkleExo. The overview of the work is presented in Fig. 1. Mainly, the contributions and innovations are as follows.

- This is the first study that uses the skeletal muscle's US imaging signals online in the real-time closed-loop control design of assistive robotic devices.
- 2) The volitional net plantarflexion torque is predicted by using an sEMG-US imaging-driven HNM, where the synthesized muscle activation signal is estimated by fusing both real-time low-sampled US imaging-derived echogenicity signals and high-sampled sEMG signals through a sequential processing algorithm-based multirate observer.
- 3) The predicted torque is implemented in an NN-based AIC-based AAN framework that automatically adjusts the BCD-AnkleExo assistance while guaranteeing the uniformly ultimately bounded stability of the overall

- closed-loop system according to the Lyapunov stability analysis.
- 4) The proposed AAN control framework is experimentally validated on five unimpaired participants when wearing the BCD-AnkleExo and walking on the treadmill. The comparison results show that the proposed control framework exhibits superior performance over a traditional AAN control approach that only uses sEMG signals, where control outcomes include joint trajectory tracking error and assistance levels from the exoskeleton.

The rest of this article is organized as follows. Section II presents the sEMG–US imaging fusion-based ankle joint volitional effort prediction based on a modified HNM. The ankle joint-exoskeleton hybrid dynamical system modeling and the development of the AIC-based AAN control framework are illustrated in Section III. Section IV shows the treadmill walking experimental study, results analysis, and discussions. Finally, Section V concludes this article.

#### II. HUMAN ANKLE JOINT VOLITIONAL EFFORT PREDICTION

In this section, we develop a plantarflexion torque prediction model by synthesizing muscle activation from sEMG- and US imaging-derived signals. The first subsection establishes a HNM-based torque prediction model that takes input from a fused muscle activation model and the second subsection presents an approach to synthesize muscle activation from high-sampled sEMG and low-sampled US imaging signals.

# A. HNM Formulation of Net Plantarflexion Torque Prediction

The main contributors to the net plantarflexion torque generation include LGS and SOL muscles. An anatomical diagram of the ankle joint musculoskeletal system is shown in Fig. 2. According to the HNM [50], [51], [52], [53], [54], the volitional net plantarflexion torque  $\tau_{\rm net}(t)$  at the ankle, when only considering LGS and SOL muscles, is given as

$$\tau_{net}(t) = \sum_{j=1}^{2} M_j(t) \tag{1}$$

where the individual torque produced by each MTU is calculated as

$$M_j(t) = F_{mt_j}(t)r_{mt_j}(t) \tag{2}$$

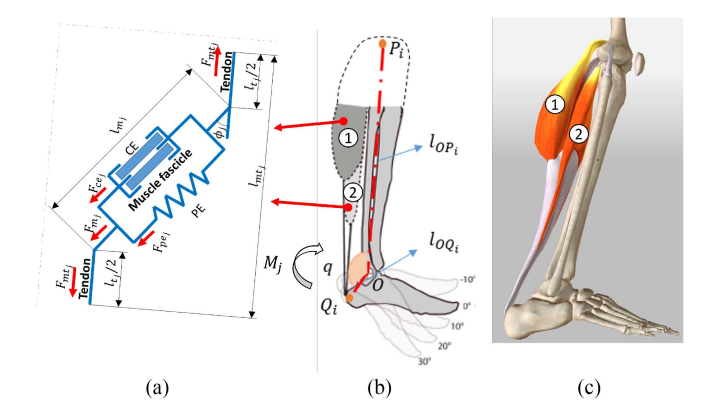


Fig. 2. Illustration of the HNM for both the LGS and SOL muscles when performing ankle plantarflexion function. (a) LGS and SOL muscles' dynamic contraction diagram. (b) Schematic representation of both LGS and SOL muscles' geometry model around the ankle joint. (c) Anatomical representation of both LGS and SOL muscles during the walking stance phase.

where  $F_{mt_j}(t) \in \mathbb{R}$  (j=1,2] represents the LGS and SOL muscles, respectively) denotes the individual contraction force applied on the corresponding MTU. It is represented as

$$F_{mt_i}(t) = (F_{ce_i}(t) + F_{pe_i}(t))\cos(\phi_i(t))$$
 (3)

where  $\phi_j(t) \in \mathbb{R}$  denotes the pennation angle that can be determined based on the method in [48].  $F_{ce_j}(t) \in \mathbb{R}$  and  $F_{pe_j}(t) \in \mathbb{R}$  denote the corresponding forces generated by the parallelly located CE and PE and can be calculated as [50], [51], [54]

$$\begin{bmatrix} F_{ce_{j}}(t) \\ F_{pe_{j}}(t) \end{bmatrix} = \begin{bmatrix} F_{j}^{\max} f_{l_{j}}(l_{m_{j}}(t)) f_{v_{j}}(v_{m_{j}}(t)) a_{j}(t) \\ F_{j}^{\max} f_{p_{j}}(l_{m_{j}}(t)) \end{bmatrix}$$
(4)

where  $F_i^{\max} \in \mathbb{R}$  denotes the muscle contraction force at maximum volitional isometric contraction, which can be referred from the literature [52], [55], [56] or identified based on an optimization algorithm in the HNM calibration procedures.  $f_{l_j}(l_{m_j}(t)), f_{v_j}(v_m(t)), \text{ and } f_{p_j}(l_{m_j}(t)) \in \mathbb{R}$  denote the generic muscle contractile force-fascicle length, force-fascicle velocity, and passive elastic force-fascicle velocity curves, respectively. These curves were normalized to  $F_j^{\max}$ , optimal fascicle length  $l_{m_j}^0 \in \mathbb{R}$ , and maximum fascicle contraction velocity  $v_{m_j}^{\max} \in \mathbb{R}$ . The values of  $l_{m_j}^0$  and  $v_{m_j}^{\max}$  were fixed and reported by Delp [55]. The explicit expressions of  $f_{l_j}(l_{m_j}(t))$ ,  $f_{v_i}(v_m(t))$ , and  $f_{p_i}(l_{m_j}(t))$  can be found in [30], [37], [54], and [57]. The CE length and velocity were determined by using data from OpenSim (National Institutes of Health for Biomedical Computation, Stanford, CA, USA) [58] and the scaling method therein. For both the LGS and SOL muscles, we built a thirdorder polynomial relationship between the CE length and the ankle joint position, as well as between the CE velocity and the ankle joint velocity, according to the data from OpenSim. These two polynomial functions were used in the HNM to determine the CE length and velocity for either LGS or SOL muscle in real-time.  $a_i(t) \in \mathbb{R}$  denotes the muscle activation that will be derived by using the proposed sEMG-US imaging fusion subsequently.

In (2),  $r_{mt_j}(t) \in \mathbb{R}$  represents the moment arm of each MTU and is calculated by using the musculoskeletal geometry model

in Fig. 2. Consider the ankle joint dorsiflexion/plantarflexion's rotation center in the sagittal plane as point O, the proximal and distal osteotendinous junction points of each MTU as  $P_j$  and  $Q_j$ , and the angle between  $OP_j$  and  $OQ_j$  as q(t). Then, each MTU length,  $l_{mt_j}(t) \in \mathbb{R}$ , is represented as the distance between  $P_j$  and  $Q_j$  and calculated based on the law of cosines as

$$l_{mt_j}(t) = \sqrt{l_{OP_j}^2 + l_{OQ_j}^2 - 2l_{OP_j}l_{OQ_j}\cos(q(t))}$$
 (5)

where  $l_{OP_j} \in \mathbb{R}$  and  $l_{OQ_j} \in \mathbb{R}$  represent the distances of  $OP_j$  and  $OQ_j$  in Fig. 2 that are obtained from OpenSim, respectively. By using the law of sines, we can derive  $r_{mt_j}(t)$  as

$$r_{mt_j}(t) = \frac{\partial l_{mt_j}(t)}{\partial (q(t))} = \frac{2l_{OP_j}l_{OQ_j}\sin(q(t))}{l_{mt_j}(t)}.$$
 (6)

#### B. Sequential Processing for the Muscle Activation Fusion

The objective of the sensor fusion is to obtain an estimation of muscle activation  $a_j(t)$  in (4), noted as  $\hat{a}_j(t)$ , by combining the sEMG-derived muscle activation,  $a_1$ , and the US imaging-derived muscle activation,  $a_2$ . Our pilot study in [37] investigated one possible way to fuse the muscle activation components from both sEMG and US imaging signals by adding an allocation ratio. The optimal allocation ratio was determined based on the HNM model calibration by using offline processed experimental data (with a lower sampling rate of 20 Hz). However, some challenges still remain to be solved, including: 1) a generalized optimal allocation ratio for different participants; 2) the online generation of US imaging-derived features; and 3) the fusion of signals with asynchronous sampling rates. To address the above challenges, we propose to use the subsequent stochastic approach to obtain the optimal estimation of muscle activation.

The discrete-time form of the first-order activation dynamics, shown in [59], can be written as

$$a_j(t_{k+1}) = A_{j,k}a_j(t_k) + B_{j,k}u_j(t_k) + v_j^*(t_k)$$
 (7)

where  $A_{j,\,k},\,B_{j,\,k}$ , and  $v_j^*(t_k)\in\mathbb{R}$  are calculated as  $A_{j,\,k}=e^{-\frac{1}{T_{a_j}}(t_{k+1}-t_k)},\,\,B_{j,\,k}=1-e^{-\frac{1}{T_{a_j}}(t_{k+1}-t_k)},\,\,$  and  $v_j^*(t_k)=\int_{t_k}^{t_{k+1}}e^{-\frac{1}{T_{a_j}}(t_{k+1}-t)}v_j(t)dt.$  Since the input of the muscle activation dynamics is from the CNS, which is very challenging to acquire directly, it is hypothesized that  $u_j(t_k)\in\mathbb{R}$  is an unknown input signal.  $T_{a_j}\in\mathbb{R}^+$  is the time constant of each muscle activation, and  $v_j(t)\in\mathbb{R}$  is assumed to be an additive white Gaussian noise signal. The index j=1,2 represents the LGS and SOL muscles, and the index  $k=1,2,\ldots$  represents the discrete sampling time instant.

The high-sampled and low-sampled muscle activation signal measurements from sEMG and US imaging are depicted in Fig. 3. The vertical orange lines represent the sEMG measurements, which are immediately available without considering delay, and the dashed blue lines represent the US imaging measurements. Here,  $t_k$  is the current measurement instant,  $t_s$  is the sampling instant for the US imaging measurement that is available at  $t_k$ ,  $h_s \in \mathbb{R}^+$  is the basic sampling interval, and  $Y^1(t_k) \in \mathbb{R}$  and  $Y^2(t_k) \in \mathbb{R}$  represent the sEMG-induced and US imaging-induced muscle activation measurements,

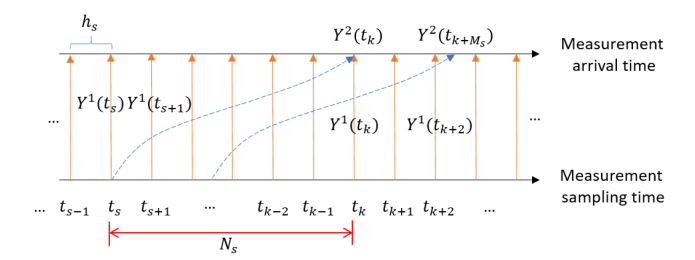


Fig. 3. Schematic of multirate and delayed muscle activation measurements from sEMG signals and US imaging.

respectively. There exists a delay  $N_s$  from the sampling instant  $t_s \in \mathbb{R}^+$  to the instant  $t_k \in \mathbb{R}^+$  when the US-derived measurement is available. The time instants when only sEMG signals are available and when both sEMG and US imaging signals are available are defined as the minor instance and major instance, respectively. The US imaging is sampled at a low rate, and the next sample is taken at  $t_s + M_s$ , where  $M_s \in \mathbb{R}^+$  is a constant number of intervals between two successive US imaging samples.

Given the description above, the measurement models for sEMG signals and US imaging are presented as

$$\begin{bmatrix} Y_j^1(t_k) \\ Y_j^2(t_k) \end{bmatrix} = \begin{bmatrix} a_j(t_k) + \nu_j^1(t_k) \\ a_j(t_s) + \nu_j^2(t_s), & \text{if } k = s + N_s \end{bmatrix}$$
(8)

where  $Y_j^1$  and  $Y_j^2$  are the normalized measurements from the sEMG linear envelope and US imaging-derived echogenicity, respectively, which will be detailed in the subsequent experimental protocol section. The noise sources  $v_j^*(t_k)$ ,  $\nu_j^1(t_k)$ , and  $\nu_j^2(t_s) \in \mathbb{R}$  are assumed to be additive white Gaussian noise signals with respective covariance matrices  $Q_j$ ,  $R_j^1$ , and  $R_j^2 \in \mathbb{R}$ .

To fuse the multirate measurements with delays, a sequential processing scheme [60] was applied here. This sequential processing occurs whenever the individual measurement from either sEMG or US imaging is available. The measurements  $Y_j^1(t_k)$  are first processed by a Kalman filter. Starting with the filtered state estimate  $\hat{a}_j^1(t_{k-1}|t_{k-1})$  and its error covariance matrix  $P_j^1(t_{k-1}|t_{k-1})$ , the state estimation at time  $t_k$  is computed recursively as

$$\hat{a}_{j}^{1}(t_{k}|t_{k-1}) = A_{j,k-1}\hat{a}_{j}^{1}(t_{k-1}|t_{k-1}) + B_{j,k}\hat{u}_{j}(t_{k-1})$$
(9)  

$$\hat{u}_{j}(t_{k}) = S_{j}(t_{k})\left(Y_{j}^{1}(t_{k}) - \hat{a}_{j}^{1}(t_{k}|t_{k-1})\right)$$
(10)  

$$\hat{a}_{j}^{1}(t_{k}|t_{k}) = \hat{a}_{j}^{1}(t_{k}|t_{k-1})$$

+  $K_{j}^{1}(t_{k}) \left( Y_{j}^{1}(t_{k}) - \hat{a}_{j}^{1}(t_{k}|t_{k-1}) \right)$  (11)

where  $S_j(t_k) \in \mathbb{R}$  is an optimal gain that is calculated iteratively based on the approach mentioned in [61, Sec. 4].  $K_j^1(t_k) \in \mathbb{R}$  is the Kalman gain for sEMG measurement and is also calculated iteratively.

At minor instances, only  $Y_j^1(t_k)$  are available, so we can set  $\hat{a}_j(t_k|t_k)=\hat{a}_j^1(t_k|t_k)$  and  $P_j(t_k|t_k)=P_j^1(t_k|t_k)$ . For a linear system, the error covariance and the Kalman gain are only dependent on the variance of the error in the measurement and not on the measured value [60]. Therefore, even though the

US imaging measurement  $Y_j^2(t_k)$  is not immediately available at time instant  $t_k$ , the error covariance and Kalman gain with respect to this measurement can still be updated as follows as soon as the US imaging is sampled:

$$K_j^2(t_k) = P_j^1(t_k|t_k) \left[ P_j^1(t_k|t_k) + R_j^2 \right]^{-1}$$
 (12)

$$P_j^2(t_k|t_k) = [I - K_j^2(t_k)] P_j^1(t_k|t_k).$$
 (13)

During the time period  $t_s$  and  $t_k$ , since  $Y_j^2(t_s)$  is not available, the state estimation continues to be updated by using only the sEMG measurements. At the major instance  $t_{s+N_s}$ , the US imaging measurements are available, and the correction term is added to the previous estimated state  $\hat{a}_j(t_k|t_k)$  as

$$\hat{a}_{j}(t_{k}|t_{k}) = \hat{a}_{j}^{1}(t_{k}|t_{k}) + \delta \hat{a}_{j}(t_{k}) \tag{14}$$

where  $\delta \hat{a}_{j}(t_{k})$  is the correction term that is defined as

$$\delta \hat{a}_j(t_k) = W_s K_j^2(t_s) \left( Y_j^2(t_k) - \hat{a}_j(t_s | t_{s-1}) \right)$$
 (15)

where  $W_s$  is an accumulated term that accounts for the delay and is calculated by

$$W_s = \prod_{i=1}^{i=N_s} \left( I - K_j^*(s+i) \right) A_{j, s+i-1}.$$
 (16)

In (16),  $K_j^*(t) \in \mathbb{R}$  is used to distinguish it from  $K_j^1(t) \in \mathbb{R}$ , where  $t \in [t_{s+1}, t_{s+N_s-1}]$ . In other words,  $K_j^*(t_k) \in \mathbb{R}$  is computed with the condition  $P_j(t_k|t_k) = P_j^2(t_k|t_k)$ , while  $K_j^1(t_k) \in \mathbb{R}$  is computed with the condition  $P_j(t_k|t_k) = P_j^1(t_k|t_k)$ . Therefore, the muscle activation state estimates in the time interval  $[t_{s+1}, t_{s+N_s-1}]$  are suboptimal, but the above correction (15) offers the optimal state estimates at the major instance. The convergence proof can be found in [60].

#### III. AAN CONTROL DEVELOPMENT

Fig. 4 presents the overall diagram of the proposed AIC-based AAN control framework for the BCD-AnkleExo with the consideration of the ankle joint volitional effort that is predicted via the sEMG-US imaging-driven HNM. The details for each component are given in the following subsections.

#### A. System Dynamics and Impedance Matching Error

The dynamics of the ankle joint with the exoskeleton are given as

$$J\ddot{q}(t) + C\dot{q}(t) + G(q(t)) + f_{dis}(t) = \tau_h(t) + \tau_m(t)$$
 (17)

where  $q(t), \dot{q}(t), \ddot{q}(t) \in \mathbb{R}$  represent the angular position, velocity, and acceleration, respectively, of the ankle joint relative to the static standing posture.  $J, C, G \in \mathbb{R}$  are the unknown system inertia, damping, and gravitational terms, respectively.  $f_{\mathrm{dis}}(t) \in \mathbb{R}$  is the combination of the unknown external disturbances and the modeling uncertainties, including the Bowden cable friction, the impact from the environment, and so on. The variable  $\tau_h(t) \in \mathbb{R}$  is the voluntary plantarflexion torque exerted by the wearer, and  $\tau_m(t) \in \mathbb{R}$  is the applied assistance torque from the BCD-AnkleExo. To facilitate the controller design and stability analysis, the following assumptions are provided.

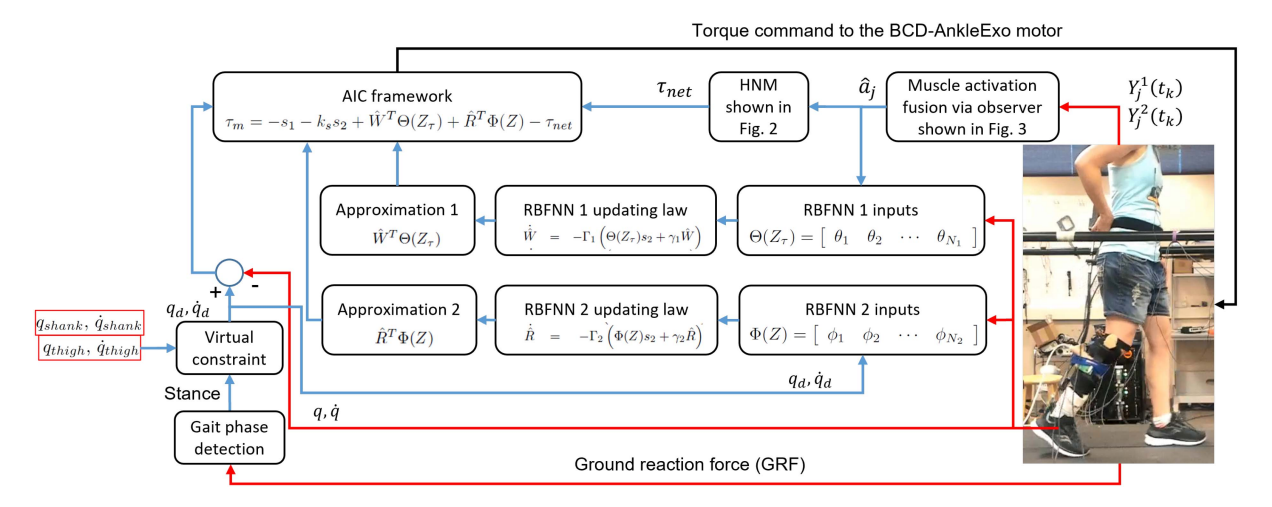


Fig. 4. Overall diagram of the AIC-based AAN control framework for the BCD-AnkleExo to provide plantarflexion assistance during the walking stance phase. The red, blue, and black lines with arrows represent the direct sensor measurements, the intermediate signals in the control system, and the torque command to the BCD-AnkleExo, respectively.

Assumption 1: The external disturbance and modeling uncertainty term  $f_{\text{dis}}$  is uniformly upper bounded by  $\bar{f} \in \mathbb{R}^+$ ,  $\forall t \in [0, \infty)$ .

Assumption 2: The unknown system inertia J is lower and upper bounded by  $\underline{J} \in \mathbb{R}^+$  and  $\overline{J} \in \mathbb{R}^+$ ,  $\forall \, t \in [0, \infty)$ , respectively.

In general, the terms J, C, and G of the overall dynamic system cannot be obtained accurately beforehand in actual applications. Thus, we introduce reference impedance parameters to the sole human ankle joint system as

$$J_d\ddot{q} + C_d\dot{q} + K_dq = \tau_h \tag{18}$$

where  $J_d$ ,  $C_d$ ,  $K_d \in \mathbb{R}^+$  are known reference inertia, damping, and stiffness coefficients of the ankle joint during the walking stance phase [62].

Define the error between the actual angular position and desired angular position as  $e=q-q_d$ , where  $q_d\in\mathbb{R}$  is continuously differentiable, bounded, and generated online based on the virtual constraints by using the shank and thigh orientations and angular velocities (see details in Appendix A). Also, the first- and second-order time derivatives of  $q_d$  are continuously differentiable and bounded. Using (18), the desired impedance model is equivalent to

$$J_d\ddot{e} + C_d\dot{e} + K_de \triangleq \tau_h - J_d\ddot{q}_d - C_d\dot{q}_d - K_dq_d. \tag{19}$$

In (19), the reference impedance model can be achieved (the RHS is equal to 0) if the real angular position q accurately tracks the desired impedance trajectory  $q_d$ . Therefore, the control objective here is to find an appropriate control input  $\tau_m$  such that the ankle joint-ankle exoskeleton dynamics mentioned in (17) can precisely match the reference model dynamics in (19).

Due to the fact that the human volitional effort  $\tau_h$  can only be predicted from the HNM, noted as  $\tau_{\rm net}$ , and because a difference exists between the system dynamics and the reference model dynamics, an impedance-matching error can be introduced as

$$\varepsilon = J_d \ddot{e} + C_d \dot{e} + K_d e - \tau_{net} + J_d \ddot{q}_d + C_d \dot{q}_d + K_d q_d \quad (20)$$

where the control objective will be fulfilled when the impedance matching error meets  $\varepsilon(t)=0$ . Since  $J_d$  is a positive constant, the newly augmented matching error can be written as

$$\varepsilon_J = \ddot{e} + C_J \dot{e} + K_J e + K_\sigma \sigma \tag{21}$$

where  $\varepsilon_J = \varepsilon/J_d$ ,  $C_J = C_d/J_d$ ,  $K_J = K_d/J_d$ ,  $K_\sigma = 1/J_d$ , and  $\sigma = J_d\ddot{q}_d + C_d\dot{q}_d + K_dq_d - \tau_{\rm net}$ .

Selecting two positive constants  $\alpha$  and  $\beta$  that satisfy the conditions  $C_J = \alpha + \beta$  and  $K_J = \alpha \beta$ , the augmented matching error is rewritten as

$$\varepsilon_J = \ddot{e} + (\alpha + \beta)\dot{e} + \alpha\beta e + \dot{\eta} + \alpha\eta \tag{22}$$

where  $\eta$  is elaborately selected to satisfy the condition that  $K_{\sigma}\sigma=\dot{\eta}+\alpha\eta$ . In addition, by defining a filtered matching error term  $r=\dot{e}+\beta e+\eta$ , we can rewrite the augmented matching error as

$$\varepsilon_J = \dot{r} + \alpha r. \tag{23}$$

# B. Neural Networks-Based Controller Development

The overall system dynamics given in (17) can be written in a state-space form as

$$\begin{bmatrix} \dot{x}_1 \\ \dot{x}_2 \end{bmatrix} = \begin{bmatrix} x_2 \\ (\tau_h + \tau_m - Cx_2 - G - f_{\text{dis}})/J \end{bmatrix}$$
 (24)

where  $[x_1, x_2]^T = [q, \dot{q}]^T$ . Defining  $\dot{q}_s = \dot{q}_d - \beta e - \eta$ , we have  $\ddot{q}_s = \ddot{q}_d - \beta \dot{e} - \dot{\eta}$ . Considering that  $r = \dot{e} + \beta e + \eta$ , we can get  $\dot{q}_s = \dot{q} - r$ , which implies  $\ddot{q}_s = \ddot{q} - \dot{r}$ . To facilitate the stability analysis, we define variables  $s_1 = x_1 - q_d = e$  and  $s_2 = x_2 - \dot{q}_s$ . Since only one degree of freedom exists in the targeted system,  $q_s \in \mathbb{R}$ ,  $s_1 \in \mathbb{R}$ , and  $s_2 \in \mathbb{R}$ .

By taking the time derivatives of  $s_1$  and  $s_2$ , we have

$$\begin{bmatrix} \dot{s}_1 \\ \dot{s}_2 \end{bmatrix} = \begin{bmatrix} s_2 - \beta e - \eta \\ (\tau_h + \tau_m - Cx_2 - G - f_{dis}) / J - \ddot{q}_s \end{bmatrix}.$$
 (25)

Considering the error between the ankle joint torque estimation  $\tau_{\rm net}$  from the sEMG-US imaging-driven HNM and the

actual exact torque  $\tau_h$  in (17), we define  $\triangle \tau = \tau_{\rm net} - \tau_h$ , which is unknown. In addition, the external disturbance and ankle exoskeleton dynamics are also unknown. Inspired by Wolbrecht et al. [23] and Li et al. [29], we exploit two Gaussian RBFNNs to represent these two unknown functions as

$$\Delta \tau = W^{*T} \Theta(Z_{\tau}) + \epsilon_{\tau} \tag{26}$$

$$Cs_2 + C\dot{q}_s + G(x_1) + J\ddot{q}_s = R^{*T}\Phi(Z) + \epsilon_e$$
 (27)

where  $W^* \in \mathbb{R}^{N_1}$  and  $R^* \in \mathbb{R}^{N_2}$  are optimal weights for the two NNs and  $N_1$  and  $N_2$  are the number of neurons in the hidden layers.  $\Theta(Z_\tau): \mathbb{R}^5 \to \mathbb{R}^{N_1}$  and  $\Phi(Z): \mathbb{R}^6 \to \mathbb{R}^{N_2}$  are the basis function matrices of the two NNs, and  $\epsilon_\tau \in \mathbb{R}$  and  $\epsilon_e \in \mathbb{R}$  are approximation errors of the two NNs, which are upper bounded by positive constants that can be written as  $|\epsilon_\tau| \leq \bar{\epsilon}_\tau$  and  $|\epsilon_e| \leq \bar{\epsilon}_e$ . The augmented input vectors for the two NNs are defined as  $Z_\tau = [1, x_1, x_2, \hat{a}_1, \hat{a}_2]^T$  and  $Z = [1, x_1, x_2, q_s, \dot{q}_s, \ddot{q}_s]^T$ .

The Gaussian radial basis functions of  $\Theta(Z_{\tau})$  and  $\Phi(Z)$  are defined as

$$\theta_{n_1} = e^{-\frac{\left\|Z_{\tau-\mu_{n_1}}^1\right\|^2}{2\delta_1^2}}, \quad \phi_{n_2} = e^{-\frac{\left\|Z_{\tau-\mu_{n_2}}^2\right\|^2}{2\delta_2^2}}$$
 (28)

where  $\mu_{n_1}^1 \in \mathbb{R}^5$   $(n_1=1,2,\ldots,N_1)$  and  $\mu_{n_2}^2 \in \mathbb{R}^6$   $(n_2=1,2,\ldots,N_2)$  are the centers of the  $n_1^{\text{th}}$  or  $n_2^{\text{th}}$  RBF with respect to the elements in  $Z_{\tau}$  or Z.  $Z_{\tau}$  and Z are the current state variables in the augmented input vectors, and  $\delta_1$  and  $\delta_2$  are scalar smoothing constants that determine the width of the basis functions. The number of basis functions and the values of  $\delta_1$  and  $\delta_2$  will be chosen experimentally to provide the best possible tradeoff between the precision of the approximation and the computational complexity of the proposed controller. Therefore, the matrices of all radial basis functions for the two NNs are defined as

$$\Theta(Z_{\tau}) = \begin{bmatrix} \theta_1 & \theta_2 & \cdots & \theta_{N_1} \end{bmatrix}^T$$

$$\Phi(Z) = \begin{bmatrix} \phi_1 & \phi_2 & \cdots & \phi_{N_2} \end{bmatrix}^T. \tag{29}$$

Based on the GRBFNNs, the unknown volitional net plantarflexion torque prediction error can be approximated as  $\hat{W}^T\Theta(Z_\tau)$ , while the external disturbance and exoskeleton dynamics can be approximated as  $\hat{R}^T\Phi(Z)$ . The vectors  $\hat{W}$  and  $\hat{R}$  are the estimates of the optimal weights for the NNs in (26) and (27), and their updating laws are designed as

$$\dot{\hat{W}} = -\Gamma_1 \left( \Theta(Z_\tau) s_2 + \gamma_1 \hat{W} \right)$$

$$\dot{\hat{R}} = -\Gamma_2 \left( \Phi(Z) s_2 + \gamma_2 \hat{R} \right)$$
(30)

where  $\gamma_1$  and  $\gamma_2$  are small positive gains and  $\Gamma_1 \in \mathbb{R}^{N_1 \times N_1}$  and  $\Gamma_2 \in \mathbb{R}^{N_2 \times N_2}$  are symmetric positive-definite matrices. The first term on the RHS of either  $\hat{W}$  or  $\hat{R}$  tends to reduce the tracking error and is a typical adaptive control term in which  $\Gamma_1$  or  $\Gamma_2$  determines the overall tracking error-based adaption rate. The second term on the RHS of either  $\hat{W}$  or  $\hat{R}$  tends to reduce the control input and preserve the system information learned from the previous motion cycle, which is essential for the repeated movement of the ankle joint during walking. We define

the optimal weights' estimation errors as  $\tilde{W} = \hat{W} - W^*$  and  $\tilde{R} = \hat{R} - R^*$ , which need to be bounded during the impedance control implementation. The updating laws proposed in (30) are supposed to achieve a decrease in the torque applied by the ankle exoskeleton when the wearer is able to complete the ankle joint movement during walking and vice versa.

The overall AAN control law (in Fig. 4) for achieving zero error between the ankle exoskeleton dynamics and the human ankle joint desired impedance model is given as

$$\tau_m = -s_1 - k_s s_2 + \hat{W}^T \Theta(Z_\tau) + \hat{R}^T \Phi(Z) - \tau_{\text{net}}.$$
 (31)

The sufficient conditions of selected control gains, i.e.,  $\beta$ ,  $k_s$ ,  $\gamma_1$ , and  $\gamma_2$ , the semiglobal boundedness of signals in the closed-loop system, i.e.,  $\Omega_{s_1}$ ,  $\Omega_{s_2}$ ,  $\Omega_{\tilde{W}}$ , and  $\Omega_{\tilde{R}}$ , and the Lyapunov stability analysis are presented in Appendix B.

### IV. EXPERIMENTAL STUDY AND RESULTS

# A. Experimental Protocol and Apparatus

The treadmill walking experimental study was approved by the IRB at North Carolina State University (IRB approval number: 20602). Five young participants (identified as A01, A02, ..., A05, three males and two females, age: 25.4±3.1 years, height: 1.77±0.10 m, and mass: 78.0±21.1 kg) with no neurological disabilities were included to conduct walking experiments at 0.60 m/s on an instrumented treadmill when wearing the designed BCD-AnkleExo. Participants signed a written informed consent form prior to the experimental sessions. The entire study included three different scenarios that are detailed below for each participant. During each scenario, we asked the participants to walk for 3 min with the first 2 min as an acclimation procedure, and the last 1 min for data collection, which was used for results' presentation and analysis in this article.

- 1) *Scenario 1 (S1):* Treadmill walking task while wearing the BCD-AnkleExo with the setting of zero impedance control mode.
- Scenario 2 (S2): Treadmill walking task while wearing the BCD-AnkleExo in the AIC mode with only sEMG-based ankle joint effort prediction.
- 3) *Scenario 3 (S3):* The similar procedures as S2 but in the proposed AIC with sEMG-US imaging-based ankle joint effort prediction.

During the treadmill walking experiments, in addition to the BCD-AnkleExo (details of the mechatronic design and benchtop testings can be seen in Appendix C), we placed 28 reflective markers (Vicon Motion System Ltd., Los Angeles, CA, USA) on the lower limbs and pelvis for the measurements of three-dimensional coordinates of each segment at 100 Hz and used them for offline ID calculation. The GRF signals from two force plates (Bertec, Columbus, OH, USA) mounted beneath the split treadmill belts were also collected at 1000 Hz for offline ID calculation. Furthermore, a threshold (5% of the z-axis GRF signal) was selected to differentiate the stance and swing phases in real time on both legs during each gait cycle, which was used to switch between two controllers, i.e., the AIC during the stance phase and a traditional proportional—derivative controller

for regulating the dorsiflexion motion during the swing phase. In this article, only results from the stance phase are presented.

Two sEMG sensors (Bagnoli<sup>TM</sup> Desktop, DELSYS, Natick, MA, USA) were attached onto both the LGS and SOL muscles to measure the corresponding sEMG signals at 1000 Hz. A linear US transducer (38 mm in length, 6.4 MHz center frequency, L7.5SC Prodigy Probe, S-Sharp, Taipei, Taiwan) was cross-sectionally attached to the location next to the sEMG sensor for the LGS muscle to image both superficial LGS and deep SOL muscles in the same plane. sEMG signals were first bandpass filtered with a bandwidth between 20 and 450 Hz, full-wave rectified and low-pass filtered with a cutoff frequency of 6 Hz, and then normalized to the peak value/contraction under scenario S1. After obtaining the normalized linear envelope, denoted as  $N_j(t_k)$ , a second-order recursive filter was used to calculate the neural activation of each muscle, denoted as  $u_j(t_k)$ , which is given by

$$u_j(t_k) = \alpha_0 N_j(t_k - \tau_j) - \beta_1 u_j(t_k - 1) - \beta_2 u_j(t_k - 2)$$

where  $\alpha_0 = 0.9486$ ,  $\beta_1 = -0.056$ , and  $\beta_2 = 0.000627$  [52].  $\tau_j$  is the EMD and is usually between 30 and 120 ms. Finally, a nonlinear relationship between the neural activation  $N_j(t_k)$  and the corresponding muscle activation, denoted as  $Y_j^1(t_k)$  in Section II-B, is given as [52]

$$Y_j^1(t_k) = \frac{e^{A_j N_j(t_k)} - 1}{e^{A_j} - 1}$$

where  $A_j$  represents the nonlinear shape factor for each muscle, which is allowed to vary between -3 and 0, with  $A_j = 0$  being a linear relationship.

The US echogenicity signals of LGS and SOL muscles at each available time instant  $t_k$  are calculated as

$$Echo_{j}(t_{k}) = \frac{1}{N_{A}N_{L}} \sum_{x=1}^{N_{A}} \sum_{y=1}^{N_{L}} I_{j,t_{k}}(x, y)$$
(32)

where  $N_A$ ,  $N_L \in \mathbb{R}^+$  represent the pixel numbers along axial and lateral directions, respectively.  $I_{j,t_k}(x,y) \in \mathbb{R}$  represents the US intensity information at the pixel location (x, y) in the region of interest from the logarithmically compressed imaging signals after the beamforming procedure. Owing to the pixel displacement tracking-free nature of the US echogenicity signal, it is the most feasible US imaging-derived feature for online feedback and implementation in the closed-loop control problem. Visually, the echogenicity signal reflects the overall brightness change of the muscle's region of interest, which linearly correlates with the muscle contraction level [38], [44]. Similarly, the US echogenicity signals from (32) were also normalized to the values between no contraction and the peak contraction in S1 to calculate the US imaging-induced muscle activation, denoted as  $Y_i^2(t_k)$  in Section II-B. Prior tests showed that the transfer rate of the real-time US echogenicity data from the US machine to the host computer running the control algorithm was around 7.8 frames/s. This implied that the US imaging-derived muscle activation measurement sampling rate was significantly lower than the sampling rates of other sensing channels for a real-time

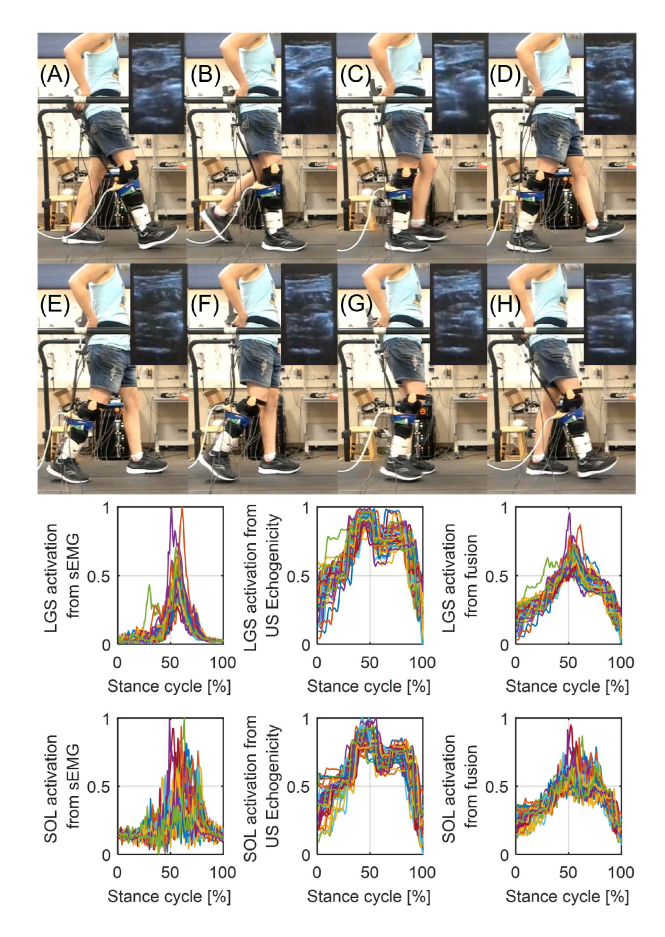


Fig. 5. Treadmill walking experimental setup and snapshots from (A) to (H) of a representative gait cycle on A02. The bottom plots demonstrate the real-time sEMG-derived muscle activation (left column), US-echogenicity-derived muscle activation (middle column), and muscle activation fusion (right column) from both LGS and SOL muscles during multiple stance cycles in S1.

control purpose, which was addressed by using the sequential processing algorithm in Section II-A.

# B. Treadmill Walking Experimental Results

1) Validation of the Sensor Fusion on the Ankle Joint Volitional Effort Prediction: The snapshots of treadmill walking experiments on one representative participant in S1 are shown on the top of Fig. 5 with a sequence from (A) to (H), where each gait cycle was defined between the current and next heel-strike instants based on the real-time GRF measurements. Readers can find more intuitive demonstrations when referring to the supplementary videos. During the demonstrated gait cycle, the corresponding B-mode US image sequences of both LGS and SOL muscles are plotted on the RHS of each snapshot and the echogenicity changes of both muscles are visualized during the stance phase. On the bottom of Fig. 5, the left column, middle column, and right column plots show the sEMG-derived muscle activation, US echogenicity-derived muscle activation, and muscle activation fusion from both LGS and SOL muscles during the walking stance phases within the last minute, respectively. The x-axis from each plot is normalized between 0% and 100% to represent the time instants of heelstrike and toe-off, namely stance phase/cycle. Recalling the net

TABLE I

MEAN AND SD VALUES OF NET PLANTARFLEXION TORQUE PREDICTION RMSE RESULTS BASED ON DIFFERENT HNMS ACROSS ALL STANCE CYCLES WITHIN THE RECORDED 1-MIN WALKING DURATION AND PEAK TORQUE FROM BENCHMARK MEASUREMENTS (UNIT: N·M)

Condition	S1				S2				S3						
Subject	sEMG		sEMG-US		Peak	sEMG		sEMG-US		Peak	sEMG		sEMG-US		Peak
Subject	Mean	SD	Mean	SD	1 Cak	Mean	SD	Mean	SD	1 can	Mean	SD	Mean	SD	1 Cak
A01	18.89	6.19	15.32*	4.01	107.08	10.53	6.69	6.91*	4.39	100.44	11.13	4.36	8.81*	3.61	107.05
A02	14.32	5.99	9.74*	4.45	106.55	14.85	5.29	10.48*	4.06	111.77	10.86	5.04	7.47*	4.96	119.97
A03	16.97	6.54	13.94*	5.43	130.26	12.41	2.32	10.18	2.68	130.05	12.06	4.09	11.05	4.06	128.11
A04	16.47	7.72	13.76*	9.61	109.48	13.19	5.94	10.46	5.28	112.79	16.37	7.09	13.25*	5.65	111.41
A05	19.64	5.48	16.16*	4.61	108.44	21.36	7.51	16.12*	6.95	126.66	24.11	8.88	19.62*	8.64	130.05

<sup>\*</sup> represents that the torque prediction RMSE when using sEMG-US-imaging-driven HNM is significantly (p-value < 0.05) less than that when using sEMG-driven HNM with respect to the given scenario and participant.

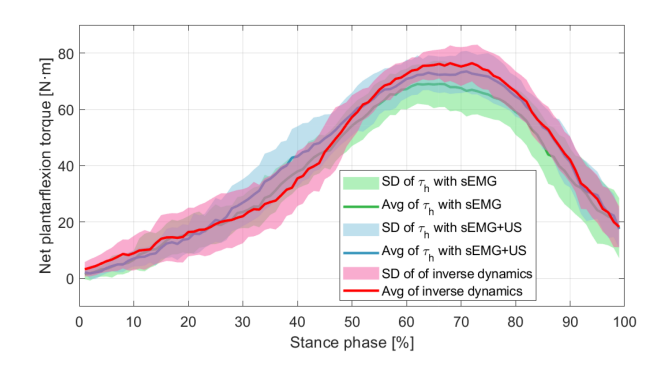


Fig. 6. Mean and SD values of the ankle joint net plantarflexion torque prediction results via sEMG- and sEMG-US imaging-driven HNMs, along with the benchmark measurement from the ID algorithm.

plantarflexion torque during the walking stance phase in [63], the change of either sEMG profiles or US echogenicity signals highly correlate to the ankle joint biological torque change during the stance phase, so the normalization of both sEMG profiles and echogenicity signals from both muscles with respect to the peak values/contractions in S1 was used in the muscle activation fusion.

The direct benefit of fusing both sEMG- and US imagingderived muscle activation signals is the higher volitional plantarflexion torque prediction accuracy. According to the treadmill walking experimental results, this benefit holds for all three scenarios and was evaluated by comparing the net plantarflexion torque prediction errors by using sEMG- and sEMG-US imaging-driven HNMs. Corresponding to the muscle activation level calculations from the neuromuscular measurements in Fig. 5, the net plantarflexion torque prediction and benchmark results are presented in Fig. 6. The benchmark results were calculated based on the ID algorithm in Visual 3D software (C-Motion, Rockville, MD, USA) given the coordinates of markers on lower extremities and GRF data. More details of the HNMs' calibration can be found in the model calibration and validation section in [48]. Considering the RMSE between torque prediction and benchmark during each stance cycle as an individual evaluation metric, the RMSE values as shown in Fig. 6 are 14.32±5.99 and 9.74±4.45 N⋅m across all stance cycles when using the sEMG- and sEMG-US imaging-driven HNMs, respectively. The averaged prediction error of the proposed HNM, when normalized to the peak value of the benchmark torque according to the ID (106.55 N·m), is around 9.2%.

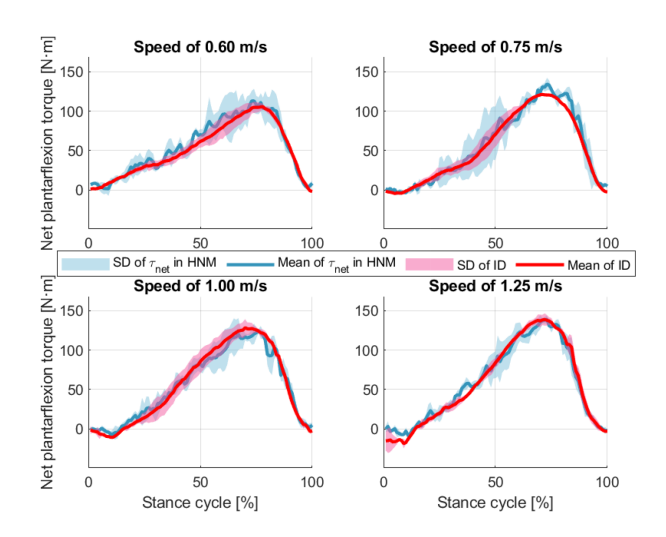


Fig. 7. Net plantarflexion torque prediction performance during the walking stance phase by using the proposed sEMG-US imaging-driven HNM in treadmill walking experiments at multiple walking speeds. The blue and red curves represent the HNM-based prediction and the benchmark results from ID, respectively.

Similar results were observed for all three scenarios from five participants, and net plantarflexion torque prediction RMSE values are summarized and compared in Table I. Except for S2 and S3 on A03 and S2 on A04, the torque prediction RMSE was significantly reduced by using the proposed sEMG-US imaging-driven HNM compared to the sEMG-driven HNM.

While the main outcomes in the current study focused on the treadmill walking experiments at a speed of 0.60 m/s, we also examined the human volitional effort (net plantarflexion torque during the walking stance phase) prediction performance of the proposed sEMG-US imaging-driven HNM in treadmill walking experiments at multiple higher walking speeds, including 0.75, 1.00, and 1.25 m/s. The representative results from participant A03 in S1 are demonstrated in Fig. 7, where blue/red solid curves and shadowed areas represent the mean and standard deviation (SD) values across multiple stance cycles within in one minute from the HNM-based prediction/ID-based calculation. The averaged prediction error normalization values are 9.1%, 8.3%, 10.3%, and 8.9%, respectively, for these four investigated speeds, which indicates that the proposed sEMG-US imaging-driven HNM achieved a good prediction performance that followed the demand for volitional net plantarflexion torque.

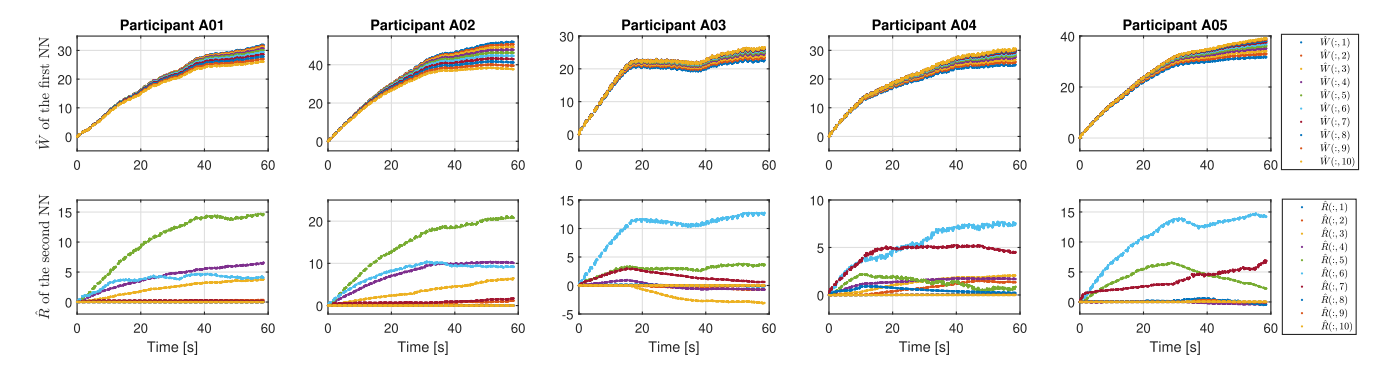


Fig. 8. Convergence results of both NN weight vectors' estimations during individual stance cycles,  $\hat{W}$  and  $\hat{R}$ , in S3 when the proposed AAN control framework is working. Each column represents the convergence performance on an individual participant, and each color in a separate plot represents the time-varying change of each element in that weight vector.

TABLE II NECESSARY DESIGN PARAMETERS AND CONTROL GAINS FOR THE PROPOSED AAN FRAMEWORK

Parameter/gain	Value	Parameter/gain	Value	
$h_s$	0.001 s	$N_1$	10	
$N_s$	0.128 s	$N_2$	10	
$M_s$	0.01 s	$\delta_1$	0.5	
$J_d$	0.15 kg·m <sup>2</sup>	$\delta_2$	1.0	
$C_d$	0.15 N·m·s/rad/kg	$\gamma_1$	0.01	
$K_d$	4.0 N·m/rad/kg	$\gamma_2$	0.02	
$\alpha$	6.8	$\Gamma_1$	$I_{10}$	
$\beta$	0.02	$\Gamma_2$	$I_{10}$	
$k_s$	2.2			

 $I_{10}$  is the  $10 \times 10$  identity matrix.

Desired trajectory Actual trajectory position [°] 10 Ankle joint 0 -10 -20 10 12 18 20 14 16 Ankle torque [N·m] 100 50 10 8 18 20 22 12 14 16 Time [s]

Fig. 9. Results of desired and actual ankle joint trajectories, volitional plantarflexion torque prediction via sEMG-US imaging-driven HNM, and assistance torque from the BCD-AnkleExo during representative stance phases in S3 on A02.

2) Outcomes With and Without AIC Frameworks: To facilitate the reproduction of these results, the necessary design parameters and control gains are summarized in Table II.

To guarantee the success and effectiveness of the NN-based AIC design, one necessary assumption is that the estimations of the NN weight vectors will converge within a finite time. Taking the experimental results in S3 as an example, Fig. 8 shows the convergence of  $\hat{W}$  and  $\hat{R}$  in (30) during each stance cycle for each participant, which indicates that almost all elements in the two weight vectors converge to corresponding stable values within the recorded 1 min. In addition, stable values for elements from  $\hat{W}$  are relatively close to each other, while the majority of elements from  $\hat{R}$  converge to somewhere close to zero.

The top plots in Fig. 9 show the ankle joint trajectory tracking performance during the walking stance phase with the proposed AIC framework in S3 (embedded with the sEMG-US imaging-driven HNM for net plantarflexion torque prediction). The sequential data of both desired (red dashed curves) and actual (blue solid curves) ankle joint trajectories are from ten consecutive stance cycles out of the 1-min data collection on participant A02. In addition, corresponding to each stance phase, the net plantarflexion torque prediction via the sEMG-US imaging-driven HNM and the assistance torque from the BCD-AnkleExo are presented at the bottom of Fig. 9. These results indicate that the proposed AAN control framework achieved a

good trajectory tracking performance, a stable net plantarflexion torque prediction performance, and an adaptive assistance level from the BCD-AnkleExo (the torque assistance profile changes in response to the torque prediction and joint angle trajectory tracking error). Across all stance cycles in the second minute under S3, the ankle joint trajectory tracking RMSE is  $4.76\pm0.42^{\circ}$ , which is acceptable since the eventual control objective of the AIC is to achieve a more natural behavior of the ankle exoskeleton instead of minimizing the trajectory tracking error. Instead of using a predefined fixed assistance torque profile like in [46], the assistance torque from the BCD-AnkleExo in this study is generated automatically from the AIC framework within each stance cycle, and it is time varying during different gait cycles, which is more adaptive to variations in gait pattern and ankle joint volitional effort. The peak assistance torque appeared between 60% and 70% of the stance cycle, which is nearly consistent with the peak voluntary plantarflexion torque prediction.

To evaluate the control performance between the proposed and traditional AIC frameworks (we adopted an sEMG-driven HNM to predict the volitional plantarflexion effort in the traditional AIC framework), metrics during each stance cycle, including trajectory tracking RMSE value, assistance torque integral, and overall assistance work, were calculated and compared based on the results in S2 and S3. Fig. 10(a) and (b)

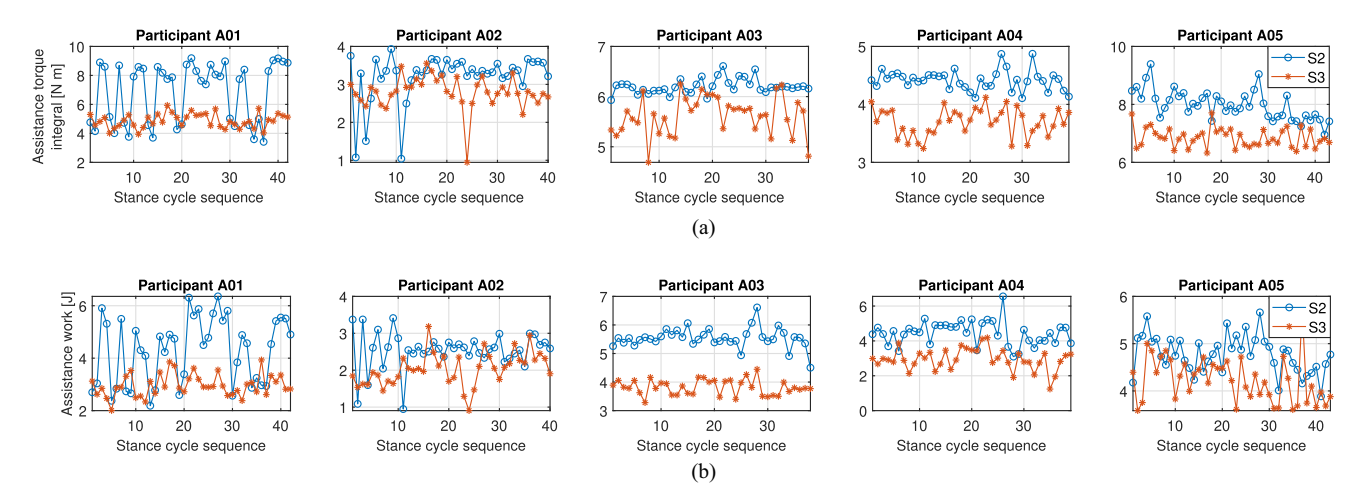


Fig. 10. Metrics of injected assistance from the BCD-AnkleExo during individual stance phases of the last minute of walking experiments in S2 and S3 on each participant. (a) Assistance torque integral during individual stance phase. (b) Overall assistance work during the individual stance phase.

shows the assistance torque integral and overall assistance work of each stance cycle at the last minute from all participants. The two metrics for evaluating the injected energy from the ankle exoskeleton in Fig. 10 indicate that the assistance during the treadmill walking stance phase was reduced for all participants when the AIC framework was incorporated with the sEMG-US imaging-driven HNM. From the individual perspective, the mean and SD values of the assistance torque integral and overall assistance work among all recorded stance cycles are presented in the middle and bottom plots of Fig. 11(a), while the mean and SD values of the trajectory tracking RMSE values in all three scenarios are shown in the top plot of Fig. 11(a). The blue, orange, and yellow bars represent the corresponding metrics' mean values under S1, S2, and S3, respectively, while the error bars represent the SD values. It should be noted that the injected assistance metrics in S1 are not shown in Fig. 11 due to the fact that zero impedance would provide minimal assistance and so can be neglected in the current work. Fig. 11(b) summarizes the interparticipant results that correspond to the individual results in Fig. 11(a) in each scenario, where the scattered points represent the mean values of each metric on individual participants across all stance cycles, and the bar plots represent the mean and SD values of each metric across all five participants.

The results of a Shapiro–Wilk parametric hypothesis test showed the normal distribution of each metric group across all stance cycles on each participant and across participants (known as interparticipant) shown in Fig. 11. A one-way repeated-measure ANOVA and a post-hoc Tukey's HSD were used to determine if there was any significant difference among the RMSE values in these three scenarios on each participant and across participants. The results in Fig. 11(a) show that both AIC frameworks significantly reduced the ankle trajectory tracking RMSE compared with S1 on each participant. In addition, the AIC framework in S3 significantly outperforms the AIC framework in S2 in terms of the trajectory tracking RMSE on all participants except for A04 (p-value =  $2.18e^{-7}$ ,  $7.21e^{-3}$ ,  $2.88e^{-2}$ ,  $5.60e^{-2}$ , and  $4.63e^{-3}$  for A01, A02,..., A05). Across all five participants, Fig. 11(b) shows the proposed AIC frameworks

in S3 and S2 significantly reduced the trajectory tracking RMSE during the stance phase by 28.42% (p-value < 0.01) and 15.56% (p-value < 0.05), respectively, when compared to results in S1. In addition, the proposed AIC framework in S3 significantly reduced the ankle joint trajectory tracking RMSE by 15.23% (p-value < 0.05) compared to the AIC framework in S2.

Furthermore, the experimental results in Fig. 11(a) show that the AIC framework in S3 significantly reduced the assistance torque integral (p-value =  $2.56e^{-8}$ ,  $2.87e^{-4}$ ,  $4.15e^{-12}$ ,  $6.17e^{-19}$ , and  $1.02e^{-15}$  for A01, A02,..., A05) and overall assistance work (p-value =  $1.62e^{-8}$ ,  $5.00e^{-3}$ ,  $2.68e^{-23}$ ,  $5.14e^{-15}$ , and  $6.28e^{-7}$  for A01, A02,..., A05) from the individual perspective compared to results in S2. Across all five participants, Fig. 11(b) shows that the proposed AIC framework in S3 significantly reduced the assistance torque integral and overall assistance work by 18.08% (p-value < 0.01) and 25.48% (p-value < 0.01), respectively. The asterisk in Fig. 11 represents the statistically significant difference at a 95% confidence level.

# C. Discussions

Rehabilitative or assistive devices can achieve a more intuitive and transparent control when applying an AAN control framework. In addition, AAN control can also encourage the wearers to actively participate in rehabilitation procedures, which is likely to maximize training benefits. The accurate determination of human joint motion intent or residual effort is essential for AAN control development. In this article, we proposed to use an sEMG-US imaging-driven HNM, a biological HMI that fuses neuromuscular signals from both sEMG and US imaging to predict human ankle joint volitional effort. We then incorporated this new HNM into an NN-based AIC framework to achieve the AAN control objective of a BCD-AnkleExo, which automatically adjusted the assistance torque from the ankle exoskeleton. The system's mechatronic performance and the controller's effectiveness were validated through treadmill walking experiments at 0.60 m/s on five participants with no neurological disabilities.

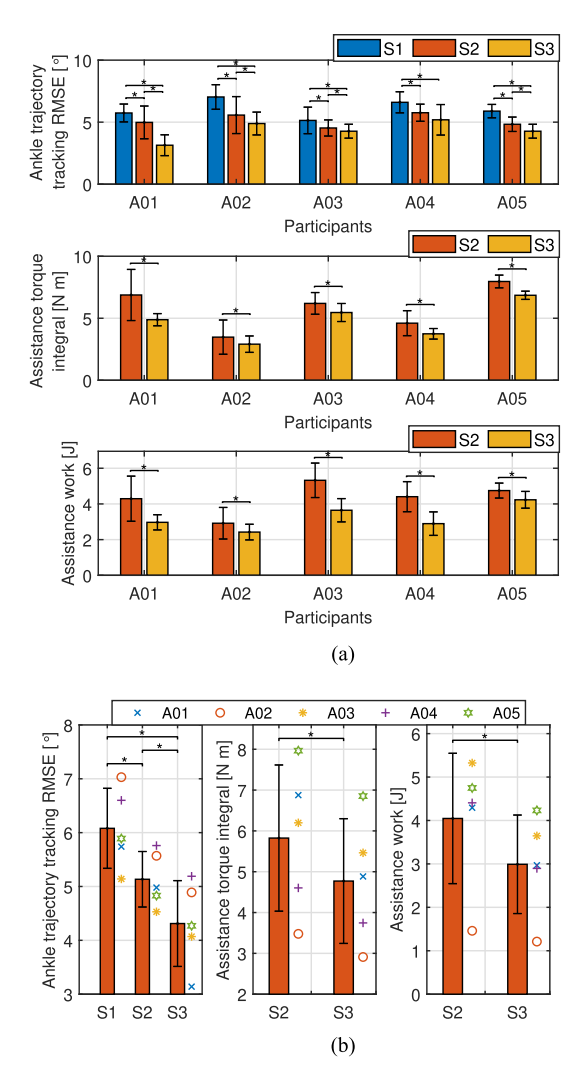


Fig. 11. Results of ankle joint trajectory tracking RMSE in three scenarios, and results of assistance torque integral and assistance work in S2 and S3 from the BCD-AnkleExo. (a) Mean and SD values of each metric across all stance phases in the corresponding scenario on each participant. (b) Intersubject statistical results of each metric across all stance phases in the corresponding scenario. The asterisk represents that the statistically significant difference is at a 95% confidence level

Given that the targeted users of the BCD-AnkleExo are individuals with residual voluntary motor control, effective controller development needs to take the human motion intent/volitional effort into consideration. Although simpler controllers that do not consider sEMG, US, HNM, or NN could estimate human motion intent by measuring mechanically intrinsic signals, including the joint angles, impedance, gait events, interaction dynamics, or estimate the joint torque from ID [37], [64], [65], [66], these mechanically intrinsic measurements are the outcomes of physical motion, which are prone to mechanical delays and may not be appropriate in some cases, as the users must produce a torque on the joints above some threshold to initiate the motion before the devices can generate assistance. Compared to the mechanically intrinsic measurements, one of the main advantages of using biological signals to estimate the motion intent/volitional effort is the time lag (between 30 and 150 ms in [44], [52], [67], [68], and [69]) between the signal generation and joint motion execution, which enables the human-intent-based control of wearable robotic devices. Specifically, the control command generation of the robotic devices advances the generation of the human joint torque or limb motion. Therefore, biological signals, especially sEMG signals, have been successfully applied in robotic devices control in the past, like examples being in [19], [26], [70], [71], [72], and [73]. The crucial perspective of the biological-signal-based control is that even if the users are not capable of producing sufficient joint motion or torque, the motion intent of the human user can still be detected, and consequently, the wearable robotic devices can be controlled.

What does the additional complexity of adding US imaging in addition to sEMG add to one or the other alone? In the current study, the US imaging was not used to track the CE length or velocity in real time due to the computationally intensive image processing procedures, which would significantly lower the sampling rate of US imaging-derived signal feedback. Instead, the echogenicity signal from US imaging was used to represent and refine the sEMG-derived muscle activation levels. We argue that both signals provide complementary information, which is beneficial to joint torque or motion prediction accuracy improvement. Our previous studies [44], [48] have shown the improvement ranges from 14% to 48% and from 28% to 54% when compared to the usage of sole sEMG or sole US imaging signals, respectively. An sEMG signal and a US imaging signal are both indirect measures of descending neural signals from the CNS. Specifically, sEMG signals measure electrical potentials generated by muscle motor units when they are neurally activated, and the amplitude of a filtered and rectified sEMG signal linearly correlates with the number of firing motor units, which offers a physical measurement of the microphysiological response [74]. Meanwhile, US imaging signals show visualized 2-D information of the macrophysiological response [75] of a targeted muscle caused by the same group of motor unit firing. Therefore, sEMG- and US imaging-derived signals provide the information from an electrical aspect and a mechanical aspect, respectively, with respect to the same physiological stimulus. Furthermore, the US echogenicity signals could provide both superficial (LGS) and deep (SOL) muscles' activation information in the same image plane on the same transducer location with less interference from adjacent muscles, while sEMG sensors would need to be placed on different locations for collecting signals from LGS and SOL muscles. The combination between sEMG and US echogenicity signals could 1) mitigate any crosstalking or interference effect from neighboring sEMG signals and 2) lower the echogenicity signals drift caused by the accumulated pixel motion and muscle tissue deformation.

The results from three scenarios demonstrated the superior performance of the proposed AAN control framework with volitional ankle joint effort prediction through the sEMG-US imaging-driven HNM, including ankle joint volitional effort prediction error reduction, trajectory tracking error reduction, and assistance torque integral and overall assistance work reduction. Although the desired ankle joint trajectory during the stance phase was generated online through virtual

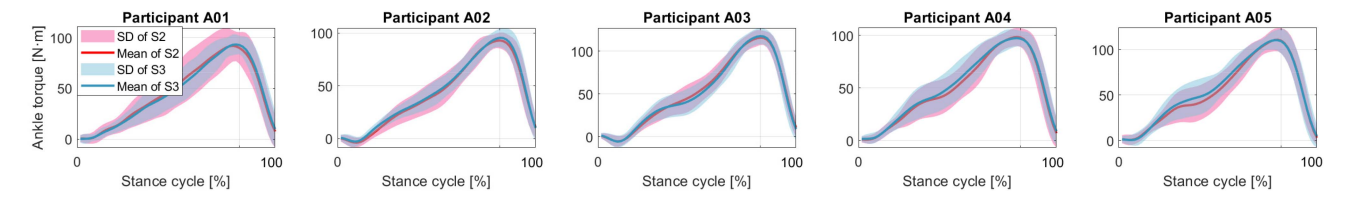


Fig. 12. Overall torque on the ankle joint under both S2 and S3 individually according to ID. The demonstrated data are from multiple gait cycles within the last minute of walking under each scenario, where the red/blue solid curves and light-shadowed areas represent the mean and SD of overall torque values under S2/S3, respectively.

constraints and varied with gait cycles and across participants due to the variations of the thigh and shank orientations and velocities, the AAN control framework maintained a relatively small trajectory tracking RMSE while providing compliant plantarflexion assistance from the exoskeleton. In addition, the volitional plantarflexion moment prediction via either the sEMG-driven or sEMG-US imaging-driven HNMs varied along with gait cycles and across participants due to the variations of sEMG and US imaging signals, but the AIC effectively regulated the assistance torque without causing discomfort to the wearers.

In this study, since participants were asked to walk on the treadmill at 0.60 m/s when wearing the BCD-AnkleExo that provided plantarflexion assistance in S2 and S3, we hypothesized that there was no obvious ankle joint torque change of the overall system due to the consistent walking speed and rhythm. By comparing the net plantarflexion torque calculated from ID in S2 and S3, we did not observe a significant difference (the relative change was under 5% of peak torque value). The results from Fig. 11 indicate that the injected torque from the BCD-AnkleExo was reduced by using the proposed AIC framework in S3 compared to the AIC framework in S2. According to the ankle joint overall net plantarflexion torque from ID, as shown in Fig. 12, the Pearson correlation coefficient (PCC) values between ankle joint trajectories within corresponding stance cycles under both S2 and S3 were calculated with the mean and SD values of  $0.967\pm0.032$ ,  $0.985\pm0.010$ ,  $0.987\pm0.011$ ,  $0.977\pm0.016$ , and 0.974±0.023 for participants A01, A02, A03, A04, and A05, respectively. From these high PCC values, we observed that the overall torque remained invariant although the assistance strategies were set differently between S2 and S3. Therefore, by subtracting the injected torque from the overall torque, the biological torque on the ankle joint volitionally generated by the participants was increased, which supported the objective of encouraging and boosting the active involvement/muscle contraction from the participants using the exoskeleton. Although these results were observed from participants without neurological disorders, they are promising and potentially translatable to people with weakened plantarflexion functions.

Despite promising results, more improvements and investigations will be of interest in future work. For example, in our current BCD-AnkleExo design, due to the space limitation on the end-effector and the application of a commercial SEA module, we did not directly get the assistance torque measurement on the ankle joint since no force or torque sensors, as mentioned in [9], [10], and [76], were installed between the cable output side and the end-effector. Instead, a transmission model was developed to

calculate the output torque on the distal cable end, as mentioned in Appendix C. However, the transmission modeling accuracy may be compromised by many unexpected factors such as the cable bending angle, the sliding of the exoskeleton attachment position, and nonlinear friction. In addition, the time-invariant reference impedance parameters referred from [62] were selected during the stance phase to simplify the AIC development and facilitate the walking task application. However, a more accurate physiologically inspired ankle exoskeleton impedance control approach should consider the time-varying properties of reference impedance parameters to accomplish a more natural walking gait pattern. Furthermore, as shown in Fig. 11, the reduction of the assistance torque integral along with individual stance phase duration by using the proposed AAN control framework may indicate that the undesired human-machine interaction was mitigated, and thus, the volitional effort from the ankle joint was boosted, which needs more investigation.

There are still some limitations in the current study. First of all, from the hardware design perspective, the BCD-AnkleExo was designed to be a portable assistive device (with lower assistance torque magnitude due to the selection of a low-power actuation module) to provide a supplementary torque upon the existing residual volitional ankle joint torque, so the BCD-AnkleExo was not able to reproduce the same torque command as the biological torque on the ankle joint during walking, like these designs in [76] and [77]. As introduced in the BCD-AnkleExo hardware design and benchtop testing section, the peak output torque from the actuator module is  $\pm 38$  N·m. With the consideration of the energy ratio through the Bowden cable transmission over a certain distance, the real assistance torque applied on the ankle joint is saturated at  $\pm 25$  N·m. Second, given the compliance of the SEA within the actuator module and the serial transmission chain design, results from benchtop testings demonstrated limited bandwidth (4.1 Hz to 2.7 Hz for torque > 12 N·m) when compared to the design in [76] and [77]. However, since the goal of the assistance level was not to reproduce the full torque command as the ankle, we interpret that the 2.7 Hz would be fairly enough for the treadmill walking task at 0.60 m/s.

Furthermore, although results in Fig. 8 showed that the convergence time of NN weights was around 40–60 s under the treadmill walking task at 0.60 m/s, we do not assume that the convergence time will be finite or the same if the walking speed or task is changed. Note that finite-time convergence of NN weights in an adaptive control design is a challenging and active research problem. In the provided stability analysis, we show that the proposed AIC framework only guarantees the uniformly

ultimately bounded stability of the overall closed-loop dynamic system, which means that the system error state exponentially converges to a bounded region. This proof does not claim that the estimated NN weights converge to their ideal weights, but the error between the ideal weight and estimated weight remains bounded. Also, note that the analysis provides sufficient conditions, which means that even if not proven, experimentally we may observe it. As seen in the experiments, NN weights converge to a steady-state value, which may or may not be ideal NN weights. In short, if the desired speed is modified we can only guarantee that the NN weights would remain bounded but do not claim convergence in finite time.

Finally, one limitation of the current experimental study design is that no experimental comparison results were included between sEMG or sEMG+US imaging and US imaging alone in the real-time control outcomes. Although the comparison of human volitional effort (joint motion or joint net torque) prediction among sEMG only, US imaging only, and sEMG+US imaging would be easier if performed offline with synchronously collected data, such as in previous studies [37], [38], [44], [48], [49], the online implementation for real-time control has two main technical challenges. First of all, the online implementation will be quite different from offline processing given that the data acquisition sampling rate of sEMG signals is much higher than that of US imaging signals, which significantly affects the data synchronization between these two sensing modalities. The computationally intensive US imaging beamforming and feature extraction cause a much lower data acquisition sampling rate for the online implementation of US imaging-based feedback. Second, the working mechanism of the applied sequential processing algorithm that tackles the data fusion between high-sampled sEMG signals (1000 Hz) and low-sampled US echogenicity signals ( $\sim$ 7.8 Hz) needs a carrier sampling rate the same as the high-sampled sEMG signals to guarantee the output of the sensor fusion with a high sampling rate (1000 Hz), which satisfies the real-time closed-loop control frequency (200 Hz). This implies that the sequential processing algorithm could still work with only sEMG signals at a high sampling rate but could not work with only US imaging signals at a low sampling rate. Although we could apply an easy approach, like zero-order hold, to process sole US imaging signals in the realtime implementation, it may significantly reduce the temporal resolution of the human effort prediction as a feedback signal for the closed-loop control problem and deteriorate the control performance.

In the current experimental study, only healthy participants were included, so no results are available related to the proposed AAN control performance on individuals with weakened ankle joint function. The next step of this study will be dedicated to the validation of the AAN control framework on participants with incomplete spinal cord injury or hemiplegia after stroke. Although the current treadmill walking experimental study focused on the stance phase, the bidirectional actuation of the ankle exoskeleton can also potentially dorsiflex the ankle joint with adequate assistance torque and bandwidth. Future work will expand the proposed AAN control to both plantarflexion and dorsiflexion assistance during the stance phase and swing phase, respectively.

#### V. CONCLUSION

In this article, for the first time, we investigated the online combination of sEMG and US imaging signals into a neuromuscular model for a continuous joint volitional effort prediction, which was incorporated with an AIC approach to achieve the AAN control of a powered ankle exoskeleton. From a real-time perspective, the online muscle activation fusion between high-sampled sEMG signals and low-sampled US imaging signals was achieved by applying a sequentialprocessing-algorithm-based multirate observer. The human volitional net plantarflexion effort was predicted via an sEMG-US imaging-driven HNM. A bioinspired AIC method that incorporated the volitional effort from the sEMG-US imaging-driven HNM was proposed and implemented on the BCD-AnkleExo for ankle joint plantarflexion assistance. The effectiveness of the hardware design and the newly proposed AAN control framework was verified on five participants with no neurological disorders walking on a treadmill. The results from three scenarios demonstrated the superior performance of the proposed AAN control framework with volitional ankle joint effort prediction through the sEMG-US imaging-driven HNM, including ankle joint volitional effort prediction error reduction, trajectory tracking error reduction, and assistance torque integral and overall injected work reduction.

# APPENDIX A DESIRED ANKLE JOINT TRAJECTORY GENERATION

For human locomotion overground or on the treadmill, due to the gait-to-gait, speed-to-speed, and person-to-person variations, the time-dependent predefined desired ankle joint trajectory during the stance phase needs to be compressed or stretched to adapt to different walking conditions or speeds, a process that is sophisticated and unreliable. Therefore, we introduce a time-independent trajectory generation profile based on virtual constraint theory [15], [78]. In the current study, the time-independent desired ankle joint trajectory was generated based on the virtual constraint theory by using the thigh, shank, and ankle joint kinematics data during the walking stance phase of the natural gait collected from individual participants walking on the treadmill at 0.60 m/s without wearing the ankle exoskeleton. Once the participant wears the ankle exoskeleton, the ankle joint kinematics will be directly affected even with the zero impedance mode, but the effects on the thigh and knee kinematics will be minor. Although the participant could generate the intended motion when wearing the ankle exoskeleton, a distinct difference was observed between free walking and zero-impedance walking. To reproduce the natural gait for the treadmill walking task, we considered the ankle joint trajectory errors between the virtual constraint-derived desired trajectory and the real ankle joint motion when designing the feedback terms in the overall AAN control framework.

Consider the term  $q_d(\theta(q)) \in \mathbb{R}$   $(q = [q_{\text{shank}}, \dot{q}_{\text{shank}}, q_{\text{thigh}}, \dot{q}_{\text{thigh}}]^T)$  as a desired virtual constraint function that is represented with the Bezier polynomial as

$$q_d(\theta(\mathbf{q})) = \sum_{k=0}^{M} \varrho_k \frac{M!}{k!(M-k)!} w^k (1-w)^{M-k}$$
 (33)

where  $M \in \mathbb{R}$  is an integer equal to the number of Bezier polynomial terms,  $\varrho_k$  represents the parameters that are determined through optimization, and w is calculated according to the following equation:

$$w(q) = \frac{\theta(q) - \theta^{+}}{\theta^{-} - \theta^{+}}$$
(34)

where  $\theta^+$  and  $\theta^-$  are the maximum and minimum values of the function  $\theta(\boldsymbol{q})$ , respectively, and  $\theta(\boldsymbol{q}) = \zeta_0 + \zeta_1 q_{\text{shank}} + \zeta_2 \dot{q}_{\text{shank}} + \zeta_3 q_{\text{thigh}} + \zeta_4 \dot{q}_{\text{thigh}}$  represents the applied phase variable.  $\zeta_i \in \mathbb{R}$  is selected such that  $\theta(\boldsymbol{q})$  is monotonically increasing or decreasing. Finally, the desired ankle joint trajectory  $q_d$  during the stance phase is set as  $q_d(\theta(\boldsymbol{q}))$ .

To obtain the optimal solution of  $\varrho_k$  in the Bezier polynomial (33), a GAPSO [79] is used to minimize the following cost function:

$$\min_{\varrho_k} J = \sum_{i=1}^{N} \left( q_d^i \left( \theta(\boldsymbol{q}) \right) - q_m^i \right)^2 \tag{35}$$

where N represents the number of data samples used in the optimization and  $q_d^i$  and  $q_m^i$  represent the Bezier polynomial-computed and measured ankle joint motion values at the ith time instant, respectively. The GAPSO utilizes kinematics data that were collected during the stance phase from able-bodied subjects at the walking speed of 0.60 m/s.

#### APPENDIX B

# STABILITY ANALYSIS OF THE CLOSED-LOOP SYSTEM

Theorem 1: Considering the ankle joint dynamic model in (17) with the human voluntary plantarflexion torque predicted from Section II, as well as the unknown external disturbance and modeling uncertainties that satisfy Assumptions 1 and 2, provided that the control gains  $\beta$ ,  $k_s$ ,  $\gamma_1$ , and  $\gamma_2$  satisfy the following sufficient conditions:

$$\beta > \frac{1}{2}, k_s > \frac{1}{2}, \gamma_1 > 0, \gamma_2 > 0$$
 (36)

the proposed AAN control approach based on the AIC framework in (31), together with NN updating laws in (30) with bounded initial weight matrices, achieve the semiglobal boundedness of signals in the closed-loop system, including  $s_1$ ,  $s_2$ ,  $\tilde{W}$ , and  $\tilde{R}$ , by compact sets of  $\Omega_{s_1}$ ,  $\Omega_{s_2}$ ,  $\Omega_{\tilde{W}}$ , and  $\Omega_{\tilde{R}}$ , given by

$$\Omega_{s_1} = \left\{ s_1 \in \mathbb{R} | |s_1| \le \sqrt{2V(0) + 2\frac{\varsigma}{\kappa}} \right\} 
\Omega_{s_2} = \left\{ s_2 \in \mathbb{R} | |s_2| \le \sqrt{\frac{2\kappa V(0) + 2\varsigma}{\kappa \underline{J}}} \right\} 
\Omega_{\tilde{W}} = \left\{ \tilde{W} \in \mathbb{R}^{N_1} | \|\tilde{W}\| \le \sqrt{\frac{2\kappa V(0) + 2\varsigma}{\kappa \lambda_{\min} \left(\Gamma_1^{-1}\right)}} \right\} 
\Omega_{\tilde{R}} = \left\{ \tilde{R} \in \mathbb{R}^{N_2} | \|\tilde{R}\| \le \sqrt{\frac{2\kappa V(0) + 2\varsigma}{\kappa \lambda_{\min} \left(\Gamma_2^{-1}\right)}} \right\}$$
(37)

where V(0) represents the initial condition of the subsequently selected Lyapunov candidate function and  $\kappa, \varsigma \in \mathbb{R}^+$  are preselected positive constant values that are used in the stability analysis. After straightforward mathematical manipulations, the impedance matching error  $\varepsilon_J$  is bounded by utilizing the proposed AAN control approach.

From the formulation of (25), the open-loop error system is provided as

$$J\dot{s}_2 = \tau_h + \tau_m - Cx_2 - G - f_{dis} - J\ddot{q}_s.$$
 (38)

Given that  $s_2 = x_2 - \dot{q}_s$  and  $\triangle \tau = \tau_{net} - \tau_h$ , the above error system becomes

$$J\dot{s}_2 = \tau_{net} - \triangle\tau + \tau_m - Cs_2 - C\dot{q}_s - G$$
$$-f_{dis} - J\ddot{q}_s. \tag{39}$$

After substituting the control law (31) and two NNs (26) and (27), the resulting closed-loop error dynamic system is given as

$$J\dot{s}_{2} = \tau_{\text{net}} - W^{*T}\Theta(Z_{\tau}) - R^{*T}\Phi(Z) - f_{\text{dis}} - \epsilon_{e} - \epsilon_{\tau}$$
$$- s_{1} - k_{s}s_{2} + \hat{W}^{T}\Theta(Z_{\tau}) + \hat{R}^{T}\Phi(Z) - \tau_{\text{net}}$$
$$= - s_{1} - k_{s}s_{2} + \tilde{W}^{T}\Theta(Z_{\tau}) + \tilde{R}^{T}\Phi(Z)$$
$$- \epsilon_{e} - \epsilon_{\tau} - f_{\text{dis}}$$
(40)

where  $\tilde{W} = \hat{W} - W^*$  and  $\tilde{R} = \hat{R} - R^*$ .

A Lyapunov-method-based stability analysis was conducted to determine the sufficient conditions and guarantee the above closed-loop error system, and the estimation errors of those two NN weight vectors,  $\tilde{W}$  and  $\tilde{R}$ , are semiglobally uniformly ultimately bounded. The proof of Theorem 1 is provided as follows.

*Proof:* Consider the continuously differentiable, nonnegative, radially unbounded Lyapunov function candidate

$$V(t) = \frac{1}{2}s_1^2 + \frac{1}{2}Js_2^2 + \frac{1}{2}\tilde{W}^T\Gamma_1^{-1}\tilde{W} + \frac{1}{2}\tilde{R}^T\Gamma_2^{-1}\tilde{R}.$$
 (41)

By using Assumption 2 and typical NN properties [80], V(t) can be lower and upper bounded as

$$\lambda_1 \|X\|^2 \le V(t) \le \lambda_2 \|X\|^2 + \zeta$$
 (42)

where  $\lambda_1$ ,  $\lambda_2$ , and  $\zeta \in \mathbb{R}^+$  are known positive constants. Among these,  $\lambda_1$  and  $\lambda_2$  are defined as  $\lambda_1 \triangleq \frac{1}{2} \min \{1, \underline{J}, \lambda_{\min}(\Gamma_1^{-1}), \lambda_{\min}(\Gamma_2^{-1})\}$  and  $\lambda_2 \triangleq \frac{1}{2} \max\{1, \overline{J}, \lambda_{\max}(\Gamma_1^{-1}), \lambda_{\max}(\Gamma_2^{-1})\}$ , respectively. In addition,  $X \in \mathbb{R}^2$  is defined as  $X = [s_1 \ s_2]^T$ .

Taking the time derivative of V and utilizing (25) and (40) yields

$$\dot{V} = s_1(s_2 - \beta e - \eta) + s_2(-s_1 - k_s s_2 - f_{dis})$$

$$+ s_2 \left( \tilde{W}^T \Theta(Z_\tau) + \tilde{R}^T \Phi(Z) - \epsilon_\tau - \epsilon_e \right)$$

$$+ \tilde{W}^T \Gamma_1^{-1} \dot{\hat{W}} + \tilde{R}^T \Gamma_2^{-1} \dot{\hat{R}}. \tag{43}$$

After applying the two NN updating laws in (30) and canceling similar terms, we have

$$\dot{V} = -\beta s_1^2 - \eta s_1 - k_s s_2^2 - s_2 \left( \epsilon_\tau + \epsilon_e + f_{\text{dis}} \right) 
- \gamma_1 \tilde{W}^T \hat{W} - \gamma_2 \tilde{R}^T \hat{R} 
\leq -\beta s_1^2 - \eta s_1 - k_s s_2^2 + |s_2| \Upsilon 
- \gamma_1 \tilde{W}^T \hat{W} - \gamma_2 \tilde{R}^T \hat{R}$$
(44)

where  $\Upsilon \in \mathbb{R}^+$  is a known positive constant and defined as  $\Upsilon \triangleq \bar{f} + \bar{\epsilon}_{\tau} + \bar{\epsilon}_{e}$ . Based on Young's inequality, we have  $-\eta s_1 \leq \frac{1}{2}\eta^2 + \frac{1}{2}s_1^2$  and  $|s_2|\Upsilon \leq \frac{1}{2}s_2^2 + \frac{1}{2}\Upsilon^2$ . In addition, since  $-\gamma_1 \tilde{W}^T \hat{W} = -\gamma_1 \tilde{W}^T (\tilde{W} + W^*)$  and  $-\gamma_1 \tilde{W}^T W^* \leq \frac{1}{2}\gamma_1 \tilde{W}^T \tilde{W} + \frac{1}{2}\gamma_1 W^{*T} W^*$ , we have  $-\gamma_1 \tilde{W}^T \hat{W} \leq -\frac{1}{2}\gamma_1 \tilde{W}^T \tilde{W} + \frac{1}{2}\gamma_1 W^{*T} W^*$ . Similarly,  $-\gamma_2 \tilde{R}^T \hat{R} \leq -\frac{1}{2}\gamma_2 \tilde{R}^T \tilde{R} + \frac{1}{2}\gamma_2 R^{*T} R^*$ . Substituting these inequalities into (44), we have

$$\dot{V} \leq -\left(\beta - \frac{1}{2}\right) s_1^2 - \left(k_s - \frac{1}{2}\right) s_2^2 + \frac{1}{2}\eta^2 + \frac{1}{2}\Upsilon^2 
- \frac{1}{2}\gamma_1 \tilde{W}^T \tilde{W} - \frac{1}{2}\gamma_2 \tilde{R}^T \tilde{R} 
+ \frac{1}{2}\gamma_1 W^{*T} W^* + \frac{1}{2}\gamma_2 R^{*T} R^*.$$
(45)

To facilitate the proposed controller in (31) to be stable, a series of conditions need to be satisfied to make (45) as a representation of  $\dot{V} \leq -\kappa V + \varsigma$ , where the two terms  $\kappa$  and  $\varsigma$  are given by

$$\kappa = \min \left\{ \beta - \frac{1}{2}, k_s - \frac{1}{2}, \frac{1}{2}\gamma_1, \frac{1}{2}\gamma_2 \right\}$$

$$\varsigma = \frac{1}{2}\eta^2 + \frac{1}{2}\Upsilon^2 + \frac{1}{2}\gamma_1 W^{*T} W^* + \frac{1}{2}\gamma_2 R^{*T} R^*. \tag{46}$$

Furthermore, to guarantee  $\kappa>0$ , the gains in (46) need to be selected as  $\beta>\frac{1}{2},\,k_s>\frac{1}{2},\,\gamma_1>0$ , and  $\gamma_2>0$ , which corresponds to the sufficient conditions in Theorem 1. Also, it is obvious that  $\varsigma\geq0$  for all the time. Therefore, the solution of the first-order differential equation  $\dot{V}\leq-\kappa V+\varsigma$  can be easily given as

$$V \le V(0)e^{-\kappa t} + \frac{\varsigma}{\kappa} \left(1 - e^{-\kappa t}\right). \tag{47}$$

Provided that the control gain  $\beta$ ,  $k_s$ ,  $\gamma_1$ , and  $\gamma_2$  are selected according to the sufficient conditions in (36), the results in (47) indicate that  $s_1(t)$ ,  $s_2(t)$ ,  $\tilde{W}(t)$ ,  $\tilde{R}(t) \in \mathcal{L}_{\infty}$ . In detail, the upper boundedness of each variable in (41) is given as

$$\begin{split} &\Omega_{s_1} = \left\{ s_1 \in \mathbb{R} | \ |s_1| \leq \sqrt{2V(0) + 2\frac{\varsigma}{\kappa}} \right\} \\ &\Omega_{s_2} = \left\{ s_2 \in \mathbb{R} | \ |s_2| \leq \sqrt{\frac{2\kappa V(0) + 2\varsigma}{\kappa \underline{J}}} \right\} \\ &\Omega_{\tilde{W}} = \left\{ \tilde{W} \in \mathbb{R}^{N_1} | \ \left\| \tilde{W} \right\| \leq \sqrt{\frac{2\kappa V(0) + 2\varsigma}{\kappa \lambda_{\min} \left(\Gamma_1^{-1}\right)}} \right\} \end{split}$$

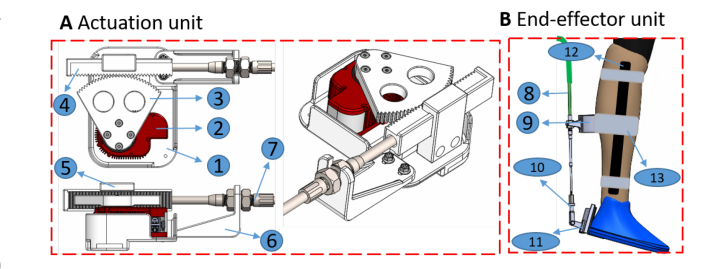


Fig. 13. 3-D model of BCD-AnkleExo. 1—base frame, 2—SEA, 3—3-D printed pinion, 4—3-D printed rack, 5—3-D printed rack track, 6—holding frame of proximal cable housing, 7—proximal cable housing, 8—distal cable housing, 9—mounting frame, 10—Clevis rod for cable output side, 11—in-shoe ankle brace and 3-D printed articular hinge, 12—supporting frame on the shank, and 13—Velcro straps.

$$\Omega_{\tilde{R}} = \left\{ \tilde{R} \in \mathbb{R}^{N_2} | \left\| \tilde{R} \right\| \le \sqrt{\frac{2\kappa V(0) + 2\varsigma}{\kappa \lambda_{\min} \left(\Gamma_2^{-1}\right)}} \right\}.$$

Given that  $q_d(t)$ ,  $\dot{q}_d(t)$ ,  $\ddot{q}_d(t) \in \mathcal{L}_{\infty}$  and considering the above boundedness conditions and (25), it is clear that e(t), r(t),  $q(t) \in \mathcal{L}_{\infty}$  since  $s_1 = e = q - q_d$ . In equation  $K_{\sigma}\sigma = \dot{\eta} + \alpha\eta$ , since  $K_{\sigma}\sigma \in \mathcal{L}_{\infty}$  and  $\alpha > 0$ , we can get  $\eta(t)$ ,  $\dot{\eta}(t) \in \mathcal{L}_{\infty}$ . Based on  $r = \dot{e} + \beta e + \eta$ , we have  $\dot{e}(t) \in \mathcal{L}_{\infty}$ . Given that  $\dot{q}_s = \dot{q}_d - \beta e - \eta$ , we have  $\dot{q}_s(t) \in \mathcal{L}_{\infty}$ . Given that  $s_2 = \dot{q} - \dot{q}_s$ , we have  $\dot{q}(t) \in \mathcal{L}_{\infty}$ . Therefore, from (18), we also have  $\ddot{q}(t) \in \mathcal{L}_{\infty}$ . From  $\ddot{q}_s = \ddot{q}_d - \beta \dot{e} - \dot{\eta}$ , it is clear that  $\ddot{q}_s \in \mathcal{L}_{\infty}$ . Finally, we have  $\dot{r}(t) \in \mathcal{L}_{\infty}$  based on the definition of  $\ddot{q}_s = \ddot{q} - \dot{r}$ , which implies that  $\varepsilon_J \in \mathcal{L}_{\infty}$  given that  $\varepsilon_J = \dot{r} + \alpha r$ . Thereafter, the impedance matching error is bounded by utilizing the proposed AAN control approach. Furthermore, since  $\tilde{W}(t)$ ,  $\tilde{R}(t) \in \mathcal{L}_{\infty}$ , the boundedness of the optimal weights [80] can be used to conclude that  $\hat{W}(t)$ ,  $\hat{R}(t) \in \mathcal{L}_{\infty}$ . Because  $s_1(t)$ ,  $s_2(t)$ ,  $\hat{W}(t)$ ,  $\hat{R}(t)$ ,  $\tau_{net}(t) \in \mathcal{L}_{\infty}$ , it can be concluded that  $\tau_m$  from the BCD-AnkleExo is bounded.

# APPENDIX C BCD-ANKLEEXO HARDWARE DESIGN AND BENCHTOP TESTING

# A. Mechatronic Design

Inspired by the biological ankle joint dorsiflexion and plantarflexion functions actuated by agonistic and antagonistic skeletal muscles on the human lower leg, we designed and constructed the BCD-AnkleExo.

The electromechanical exoskeleton system comprises an onboard actuation unit and an instrumented end-effector unit, as shown in Fig. 13. The overall mass of both units is 2.52 kg, and all components are portable except for the power and communication cables on the actuation unit. A clamp-mount low-friction *Push–Pull* Bowden cable transfers motion and power from the actuation unit (a) to the end-effector unit (b) for the dorsiflexion and plantarflexion assistance.

In the actuation unit shown in Fig. 13(a), a compact low-inertial electrical actuator module (X8-16, HEBI Robotics, Pittsburgh, PA, USA), with embedded position, velocity, and torque control modes, was used. This actuator module is a smart SEA with a spring stiffness of 170 N·m/rad that integrates a brushless

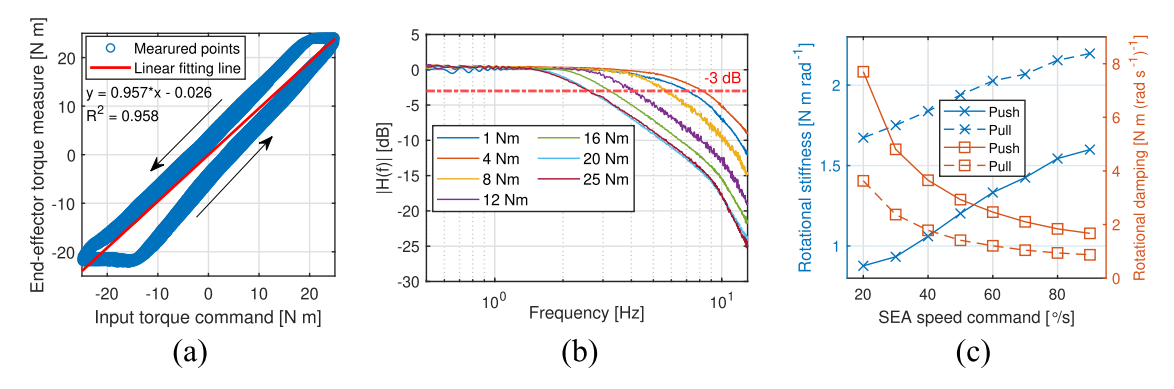


Fig. 14. Experimental results from benchtop tests of the BCD-AnkleExo prototype. (a) Torque measurement accuracy results. (b) Bode plots—the frequency response of the system with peak desired torques changing from 1 to 25 N·m. (c) Rotational stiffness  $K_r$  and damping  $C_r$  of the cable housing at different SEA speed control commands.

motor, gear train, spring, encoder, and control electronics into a compact package that runs on standard dc voltages. Desired control commands (position, velocity, or torque) are generated using a real-time MATLAB programming environment. The SEA's maximum output velocity is  $90^{\circ}$ /s after the 1462:1 gear train reduction, and peak output torque is  $38~\rm N\cdot m$ . The rotation motion (torque) of the SEA is transferred to the linear motion (force) of the steel cable through a rack-pinion transmission mechanism. The rotation radius of the pinion is designed as  $100~\rm mm$  to gain satisfactory linear speed of the cable for walking.

As shown in Fig. 13(b), we adopted a lightweight design for the end-effector unit, where the distal cable housing is mounted on the 3-D printed mounting frame and the mounting frame is connected to the participant's shank through medial and lateral rigid supporting frames and three pieces of soft velcro straps. The inner cable end is screwed into the clevis rod, which is connected to the in-shoe ankle brace through a 3-D printed articular hinge. We assumed that the distal cable end keeps a linear motion along the center line, and the moment arm is consistent as the biological ankle joint motion during walking is sufficiently small ( $\sim 20^{\circ}$  of peak plantarflexion to  $\sim 7^{\circ}$  of peak dorsiflexion) [63]. To facilitate the 1:1 transmission, the articular hinge was designed to keep the moment arm at 100 mm.

The rotation position, velocity, and output torque of the SEA were directly measured by the embedded sensors at 1000 Hz. The ankle joint position and velocity were measured by an incremental encoder (1024 pulses per revolution, TRD-MX1024BD, AutomationDirect, Cumming, GA, USA) installed on the ankle brace at 1000 Hz. The output torque of the end-effector was computed by multiplying the force on the distal cable end and the end-effector's moment arm mentioned above.

#### B. Results of Benchtop Testings

Multiple tests were performed for characterizing the BCD-AnkleExo performance in terms of output peak torque, torque measurement accuracy, and closed-loop torque control bandwidth. The outcomes of each test are given as follows.

1) Under the fixed end-effector configuration, the input torque command for both rotation directions of the SEA,  $\tau_{\text{SEA}}$ , was increased continuously from 0 N·m until the moment that the gear tooth skipping happened.

- The corresponding torque command was regarded as the input saturation. The results showed that the range of  $\tau_{SEA}$  is between  $\pm 25~{\rm N\cdot m}$ .
- 2) Under the fixed end-effector configuration,  $\tau_{\rm SEA}$  was set with the amplitude of 25 N·m and frequency of 1.0 Hz, and the output torque on the end-effector,  $\tau_m$ , was measured through the multiplication of a load cell measurement (LC201-300, Omega Engineering Inc., Norwalk, CT, USA) and a moment arm. The relationship between the sinusoidal SEA input torque command and the measured torque at the end-effector is shown in Fig. 14(a). Although hysteresis is observed between the input torque command and the end-effector output torque signal due to the elastic element in the SEA module, the two signals exhibit a highly linear correlation with  $R^2$  of 0.958 and a small RMSE of 3.78 N·m.
- 3) Under the fixed end-effector configuration, a series of chirp desired  $\tau_{\rm SEA}$  with different peak torque values and increasing frequencies between 0 and 20 Hz were applied to characterize the torque control bandwidth of the transmission design. A fast Fourier transform was applied to the chirp-type  $\tau_{\rm SEA}$  and  $\tau_m$  signals to mathematically evaluate the end-effector's response in the frequency domain and calculate the device's response magnitude. Fig. 14(b) shows the torque control bandwidths based on the -3-dB magnitude criteria, and they are 7.2, 8.3, 5.7, 4.1, 3.3, 2.7, and 2.7 Hz for peak torques of 1, 4, 8, 12, 16, 20, and 25 N·m, respectively.
- 4) Under the free end-effector configuration, the rotation speed for both directions of the SEA was increased from  $20^{\circ}/\mathrm{s}$  to the peak speed value to characterize the overall rotational stiffness  $K_r$  and damping  $C_r$  of the Bowden cable transmission approach. The results of this free end-effector test are shown in Fig. 14(c), which indicates that the stiffness and damping coefficients are asymmetric in the pull and push directions, and the stiffness and damping coefficients in both directions are positively and negatively proportional to SEA speed commands, respectively. Using the test results depicted in Fig. 14, the relationship between the output of end-effector  $\tau_m$  and the SEA input command  $\tau_{\text{SEA}}$  can be determined as  $\tau_{\text{SEA}} = (\tau_m + K_r q + C_r \dot{q})/0.958$ .

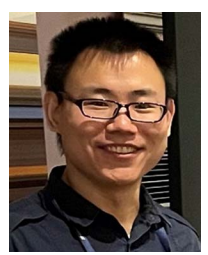
#### REFERENCES

- P. H. Tzu-wei, K. A. Shorter, P. G. Adamczyk, and A. D. Kuo, "Mechanical and energetic consequences of reduced ankle plantar-flexion in human walking," *J. Exp. Biol.*, vol. 218, no. 22, pp. 3541–3550, 2015.
- [2] L. I. Iezzoni, E. P. McCarthy, R. B. Davis, and H. Siebens, "Mobility difficulties are not only a problem of old age," *J. Gen. Intern. Med.*, vol. 16, no. 4, pp. 235–243, 2001.
- [3] K. Z. Takahashi, M. D. Lewek, and G. S. Sawicki, "A neuromechanics-based powered ankle exoskeleton to assist walking post-stroke: A feasi-bility study," *J. Neuroeng. Rehabil.*, vol. 12, no. 1, 2015, Art. no. 23.
- [4] Z. F. Lerner et al., "An untethered ankle exoskeleton improves walking economy in a pilot study of individuals with cerebral palsy," *IEEE Trans. Neural Syst. Rehabil. Eng.*, vol. 26, no. 10, pp. 1985–1993, Oct. 2018.
- [5] F. Tamburella et al., "Neuromuscular controller embedded in a powered ankle exoskeleton: Effects on gait, clinical features and subjective perspective of incomplete spinal cord injured subjects," *IEEE Trans. Neural Syst. Rehabil. Eng.*, vol. 28, no. 5, pp. 1157–1167, May 2020.
- [6] A. J. Young and D. P. Ferris, "State of the art and future directions for lower limb robotic exoskeletons," *IEEE Trans. Neural Sys. Rehabil. Eng.*, vol. 25, no. 2, pp. 171–182, Feb. 2017.
- [7] J. Zhang et al., "Human-in-the-loop optimization of exoskeleton assistance during walking," *Science*, vol. 356, no. 6344, pp. 1280–1284, 2017.
- [8] M. Kim and S. H. Collins, "Once-per-step control of ankle push-off work improves balance in a three-dimensional simulation of bipedal walking," *IEEE Trans. Robot.*, vol. 33, no. 2, pp. 406–418, Apr. 2017.
- [9] B. Quinlivan et al., "Assistance magnitude versus metabolic cost reductions for a tethered multiarticular soft exosuit," *Sci. Robot.*, vol. 2, no. 2, 2017, Art. no. eaah 4416.
- [10] A. T. Asbeck, S. M. De Rossi, K. G. Holt, and C. J. Walsh, "A biologically inspired soft exosuit for walking assistance," *Int. J. Rob. Res.*, vol. 34, no. 6, pp. 744–762, 2015.
- [11] A. J. Del-Ama, Á. Gil-Agudo, J. L. Pons, and J. C. Moreno, "Hybrid FES-robot cooperative control of ambulatory gait rehabilitation exoskeleton," J. Neuroeng. Rehabil., vol. 11, no. 1, 2014, Art. no. 27.
- [12] K. H. Ha, S. A. Murray, and M. Goldfarb, "An approach for the cooperative control of FES with a powered exoskeleton during level walking for persons with paraplegia," *IEEE Trans. Neural Syst. Rehabil. Eng.*, vol. 24, no. 4, pp. 455–466, Apr. 2016.
- [13] N. A. Alibeji, V. Molazadeh, F. Moore-Clingenpeel, and N. Sharma, "A muscle synergy-inspired control design to coordinate functional electrical stimulation and a powered exoskeleton: Artificial generation of synergies to reduce input dimensionality," *IEEE Control Syst. Mag.*, vol. 38, no. 6, pp. 35–60, Dec. 2018.
- [14] N. Kirsch, X. Bao, N. Alibeji, B. Dicianno, and N. Sharma, "Model-based dynamic control allocation in a hybrid neuroprosthesis," *IEEE Trans. Neural Syst. Rehabil. Eng.*, vol. 26, no. 1, pp. 224–232, Jan. 2018.
- [15] V. Molazadeh, Q. Zhang, X. Bao, and N. Sharma, "An iteratively learning time-invariant controller for a switched cooperative allocation strategy during sit-to-stand task with a hybrid exoskeleton," *IEEE Trans. Control Syst. Technol.*, vol. 30, no. 3, pp. 1021–1036, Jul. 2021.
- [16] Y. Ding, M. Kim, S. Kuindersma, and C. J. Walsh, "Human-in-the-loop optimization of hip assistance with a soft exosuit during walking," *Sci. Robot.*, vol. 3, no. 15, 2018, Art. no. eaar5438.
- [17] C. Khazoom, C. Véronneau, J.-P. L. Bigué, J. Grenier, A. Girard, and J.-S. Plante, "Design and control of a multifunctional ankle exoskeleton powered by magnetorheological actuators to assist walking, jumping, and landing," *IEEE Robot. Autom. Lett.*, vol. 4, no. 3, pp. 3083–3090, Jul. 2019.
- [18] J. Kim et al., "Reducing the metabolic rate of walking and running with a versatile, portable exosuit," *Science*, vol. 365, no. 6454, pp. 668–672, 2019.
- [19] R. W. Jackson and S. H. Collins, "Heuristic-based ankle exoskeleton control for co-adaptive assistance of human locomotion," *IEEE Trans. Neural Syst. Rehabil. Eng.*, vol. 27, no. 10, pp. 2059–2069, Aug. 2019.
- [20] L. Marchal-Crespo and D. J. Reinkensmeyer, "Review of control strategies for robotic movement training after neurologic injury," *J. Neuroeng. Rehabil.*, vol. 6, no. 1, pp. 1–15, 2009.
- [21] S. A. Murray, K. H. Ha, C. Hartigan, and M. Goldfarb, "An assistive control approach for a lower-limb exoskeleton to facilitate recovery of walking following stroke," *IEEE Trans. Neural Syst. Rehabil. Eng.*, vol. 23, no. 3, pp. 441–449, Aug. 2014.
- [22] L. N. Awad et al., "A soft robotic exosuit improves walking in patients after stroke," Sci. Transl. Med., vol. 9, no. 400, 2017, Art. no. eaai 9084.
- [23] E. T. Wolbrecht, V. Chan, D. J. Reinkensmeyer, and J. E. Bobrow, "Optimizing compliant, model-based robotic assistance to promote neurorehabilitation," *IEEE Trans. Neural Sys. Rehabil. Eng.*, vol. 16, no. 3, pp. 286–297, Jun. 2008.

- [24] S. Hussain, P. K. Jamwal, M. H. Ghayesh, and S. Q. Xie, "Assist-as-needed control of an intrinsically compliant robotic gait training orthosis," *IEEE Trans. Ind. Electron.*, vol. 64, no. 2, pp. 1675–1685, Feb. 2017.
- [25] H. J. Asl, T. Narikiyo, and M. Kawanishi, "Adaptive neural network-based saturated control of robotic exoskeletons," *Nonlinear Dyn.*, vol. 94, no. 1, pp. 123–139, 2018.
- [26] J. R. Koller, D. A. Jacobs, D. P. Ferris, and C. D. Remy, "Learning to walk with an adaptive gain proportional myoelectric controller for a robotic ankle exoskeleton," *J. Neuroeng. Rehabil.*, vol. 12, no. 1, 2015, Art. no. 97.
- [27] J. R. Koller, C. D. Remy, and D. P. Ferris, "Biomechanics and energetics of walking in powered ankle exoskeletons using myoelectric control versus mechanically intrinsic control," *J. Neuroeng. Rehabil.*, vol. 15, no. 1, 2018, Art. no. 42.
- [28] E. M. McCain et al., "Mechanics and energetics of post-stroke walking aided by a powered ankle exoskeleton with speed-adaptive myoelectric control," *J. Neuroeng. Rehabil.*, vol. 16, no. 1, 2019, Art. no. 57.
- [29] Z. Li, Z. Huang, W. He, and C.-Y. Su, "Adaptive impedance control for an upper limb robotic exoskeleton using biological signals," *IEEE Trans. Ind. Electron.*, vol. 64, no. 2, pp. 1664–1674, Feb. 2017.
- [30] D. Ao, R. Song, and J. Gao, "Movement performance of human-robot cooperation control based on EMG-driven hill-type and proportional models for an ankle power-assist exoskeleton robot," *IEEE Trans. Neural Syst. Rehabil. Eng.*, vol. 25, no. 8, pp. 1125–1134, Aug. 2017.
- [31] Y. Zhuang, S. Yao, C. Ma, and R. Song, "Admittance control based on EMG-driven musculoskeletal model improves the human–robot synchronization," *IEEE Trans. Ind. Informat.*, vol. 15, no. 2, pp. 1211–1218, Feb. 2019.
- [32] G. Durandau, W. F. Rampeltshammer, H. van der Kooij, and M. Sartori, "Neuromechanical model-based adaptive control of bilateral ankle exoskeletons: Biological joint torque and electromyogram reduction across walking conditions," *IEEE Trans. Robot.*, vol. 38, no. 3, pp. 1380–1394, Jun. 2022.
- [33] K. Gui, H. Liu, and D. Zhang, "A practical and adaptive method to achieve EMG-based torque estimation for a robotic exoskeleton," *IEEE/ASME Trans. Mechatronics*, vol. 24, no. 2, pp. 483–494, Apr. 2019.
- [34] K. Gui, U.-X. Tan, H. Liu, and D. Zhang, "Electromyography-driven progressive assist-as-needed control for lower limb exoskeleton," *IEEE Trans. Med. Robot. Bionics.*, vol. 2, no. 1, pp. 50–58, Feb. 2020.
- [35] J.-J. E. Slotine and W. Li, Applied Nonlinear Control, vol. 199. Englewood Cliffs, NJ, USA: Prentice-Hall, 1991.
- [36] D. L. Crouch, L. Pan, W. Filer, J. W. Stallings, and H. Huang, "Comparing surface and intramuscular electromyography for simultaneous and proportional control based on a musculoskeletal model: A pilot study," *IEEE Trans. Neural Syst. Rehabil. Eng.*, vol. 26, no. 9, pp. 1735–1744, Jul. 2018.
- [37] Q. Zhang, K. Kim, and N. Sharma, "Prediction of ankle dorsiflexion moment by combined ultrasound sonography and electromyography," *IEEE Trans. Neural Syst. Rehabil. Eng.*, vol. 28, no. 1, pp. 318–327, Nov. 2020.
- [38] Q. Zhang, A. Iyer, K. Kim, and N. Sharma, "Evaluation of non-invasive ankle joint effort prediction methods for use in neurorehabilitation using electromyography and ultrasound imaging," *IEEE Trans. Biomed. Eng.*, vol. 68, no. 3, pp. 1044–1055, Mar. 2021.
- [39] P. Hodges, L. Pengel, R. Herbert, and S. Gandevia, "Measurement of muscle contraction with ultrasound imaging," *Muscle Nerve*, vol. 27, no. 6, pp. 682–692, 2003.
- [40] S. Sikdar et al., "Novel method for predicting dexterous individual finger movements by imaging muscle activity using a wearable ultrasonic system," *IEEE Trans. Neural Syst. Rehabil. Eng.*, vol. 22, no. 1, pp. 69–76, Jan. 2014.
- [41] E. N. Wilhelm, A. Rech, F. Minozzo, R. Radaelli, C. E. Botton, and R. S. Pinto, "Relationship between quadriceps femoris echo intensity, muscle power, and functional capacity of older men," *Age*, vol. 36, pp. 1113–1122, 2014.
- [42] K. G. Rabe, T. Lenzi, and N. P. Fey, "Performance of sonomyographic and electromyographic sensing for continuous estimation of joint torque during ambulation on multiple terrains," *IEEE Trans. Neural Syst. Rehabil. Eng.*, vol. 29, pp. 2635–2644, Dec. 2021.
- [43] Z. Sheng, N. Sharma, and K. Kim, "Quantitative assessment of changes in muscle contractility due to fatigue during NMES: An ultrasound imaging approach," *IEEE Trans. Biomed. Eng.*, vol. 67, no. 3, pp. 832–841, Mar. 2020.
- [44] Q. Zhang, A. Iyer, Z. Sun, K. Kim, and N. Sharma, "A dual-modal approach using electromyography and sonomyography improves prediction of dynamic ankle movement: A case study," *IEEE Trans. Neural Syst. Rehabil. Eng.*, vol. 29, pp. 1944–1954, Nov. 2021.

- [45] R. J. Cunningham and I. D. Loram, "Estimation of absolute states of human skeletal muscle via standard B-mode ultrasound imaging and deep convolutional neural networks," *J. Roy. Soc. Interface*, vol. 17, no. 162, 2020, Art. no. 20190715.
- [46] R. Nuckols, S. Lee, K. Swaminathan, D. Orzel, R. Howe, and C. Walsh, "Individualization of exosuit assistance based on measured muscle dynamics during versatile walking," *Sci. Robot.*, vol. 6, no. 60, 2021, Art. no. eabj 1362.
- [47] Y. Fang, N. Hettiarachchi, D. Zhou, and H. Liu, "Multi-modal sensing techniques for interfacing hand prostheses: A review," *IEEE Sens. J.*, vol. 15, no. 11, pp. 6065–6076, Nov. 2015.
- [48] Q. Zhang, N. Fragnito, J. Franz, and N. Sharma, "Fused ultrasound and electromyography-driven neuromuscular model to improve plantarflexion moment prediction across multiple walking speeds," *J. Neuroeng. Rehabil.*, vol. 86, no. 19, 2022, Art. no. 86.
- [49] K. G. Rabe and N. P. Fey, "Evaluating electromyography and sonomyography sensor fusion to estimate lower-limb kinematics using gaussian process regression," Front. Robot. AI, vol. 9, 2022, Art. no. 716545.
- [50] A. V. Hill, "The heat of shortening and the dynamic constants of muscle," *Philos. Trans. R. Soc. London, B., Biol. Sci.*, vol. 126, no. 843, pp. 136–195, 1938.
- [51] F. E. Zajac, "Muscle and tendon: Properties, models, scaling, and application to biomechanics and motor control," *Crit. Rev. Biomed. Eng.*, vol. 17, no. 4, pp. 359–411, 1989.
- [52] D. G. Lloyd and T. F. Besier, "An EMG-driven musculoskeletal model to estimate muscle forces and knee joint moments in vivo," *J. Biomech.*, vol. 36, no. 6, pp. 765–776, 2003.
- [53] T. S. Buchanan, D. G. Lloyd, K. Manal, and T. F. Besier, "Neuromusculoskeletal modeling: Estimation of muscle forces and joint moments and movements from measurements of neural command," *J. Appl. Biomech.*, vol. 20, no. 4, pp. 367–395, 2004.
- [54] M. F. Eilenberg, H. Geyer, and H. Herr, "Control of a powered ankle–foot prosthesis based on a neuromuscular model," *IEEE Trans. Neural Syst. Rehabil. Eng.*, vol. 18, no. 2, pp. 164–173, Jan. 2010.
- [55] S. L. Delp, Surg. Simul.: A Computer Graph. System to Analyze and Des. Musculoskelet. Reconstructions of the Lower Limb. Redwood City, CA, USA: Stanford Univ., 1990.
- [56] L. F. de Oliveira and L. L. Menegaldo, "Individual-specific muscle maximum force estimation using ultrasound for ankle joint torque prediction using an EMG-driven hill-type model," *J. Biomech.*, vol. 43, no. 14, pp. 2816–2821, 2010.
- [57] T. J. M. Dick, A. A. Biewener, and J. M. Wakeling, "Comparison of human gastrocnemius forces predicted by hill-type muscle models and estimated from ultrasound images," *J. Exp. Biol.*, vol. 220, no. 9, pp. 1643–1653, 2017.
- [58] S. L. Delp et al., "OpenSim: Open-source software to create and analyze dynamic simulations of movement," *IEEE Trans. Biomed. Eng.*, vol. 54, no. 11, pp. 1940–1950, Nov. 2007.
- [59] N. Kirsch, N. Alibeji, and N. Sharma, "Nonlinear model predictive control of functional electrical stimulation," *Control Eng. Pract.*, vol. 58, pp. 319–331, 2017.
- [60] H. L. Alexander, "State estimation for distributed systems with sensing delay," *Proc. SPIE*, vol. 1470, pp. 103–111, 1991.
- [61] S. Gillijns and B. De Moor, "Unbiased minimum-variance input and state estimation for linear discrete-time systems with direct feedthrough," *Automatica*, vol. 43, no. 5, pp. 934–937, 2007.
- [62] E. J. Rouse, L. J. Hargrove, E. J. Perreault, and T. A. Kuiken, "Estimation of human ankle impedance during the stance phase of walking," *IEEE Trans. Neural Sys. Rehabil. Eng.*, vol. 22, no. 4, pp. 870–878, 2014
- [63] D. A. Winter, Biomechanics and Motor Control of Human Movement. Hoboken, NJ, USA: Wiley, 2009.
- [64] J. Blaya and H. Herr, "Adaptive control of a variable-impedance ankle-foot orthosis to assist drop-foot gait," *IEEE Trans. Neural Syst. Rehabil. Eng.*, vol. 12, no. 1, pp. 24–31, Mar. 2004.
- [65] S. K. Banala, S. H. Kim, S. K. Agrawal, and J. P. Scholz, "Robot assisted gait training with active leg exoskeleton (ALEX)," *IEEE Trans. Neural* Syst. Rehabil. Eng., vol. 17, no. 1, pp. 2–8, Mar. 2009.
- [66] R. Jiménez-Fabián and O. Verlinden, "Review of control algorithms for robotic ankle systems in lower-limb orthoses, prostheses, and exoskeletons," *Med. Eng. Phys.*, vol. 34, no. 4, pp. 397–408, 2012.
- [67] S. Zhou, D. L. Lawson, W. E. Morrison, and I. Fairweather, "Electromechanical delay in isometric muscle contractions evoked by voluntary, reflex and electrical stimulation," *Eur. J. Appl. Physiol. Occupat. Physiol.*, vol. 70, no. 2, pp. 138–145, 1995.

- [68] J. T. Blackburn, D. R. Bell, M. F. Norcross, J. D. Hudson, and L. A. Engstrom, "Comparison of hamstring neuromechanical properties between healthy males and females and the influence of musculotendinous stiffness," *J. Electromyography Kinesiol.*, vol. 19, no. 5, pp. e362–e369, 2009.
- [69] H. Begovic, G.-Q. Zhou, T. Li, Y. Wang, and Y.-P. Zheng, "Detection of the electromechanical delay and its components during voluntary isometric contraction of the quadriceps femoris muscle," *Front. Physiol.*, vol. 5, 2014. Art. no. 494.
- [70] H. Kawamoto and Y. Sankai, "Comfortable power assist control method for walking aid by HAL-3," in *Proc. IEEE Int. Conf. Syst.*, *Man, Cybern.*, 2002, vol. 4, p. 6.
- [71] C. Fleischer and G. Hommel, "A human–exoskeleton interface utilizing electromyography," *IEEE Trans. Robot.*, vol. 24, no. 4, pp. 872–882, Aug. 2008.
- [72] T. Lenzi, S. M. M. De Rossi, N. Vitiello, and M. C. Carrozza, "Intention-based EMG control for powered exoskeletons," *IEEE Trans. Biomed. Eng.*, vol. 59, no. 8, pp. 2180–2190, Aug. 2012.
- [73] L. Peternel, T. Noda, T. Petrič, A. Ude, J. Morimoto, and J. Babič, "Adaptive control of exoskeleton robots for periodic assistive behaviours based on EMG feedback minimisation," *PLoS One*, vol. 11, no. 2, 2016, Art. no. e0148942.
- [74] M. Barbero, R. Merletti, and A. Rainoldi, Atlas of Muscle Innervation Zones: Understanding Surface Electromyography and Its Applications. New York, NY, USA: Springer, 2012.
- [75] P. Aagaard et al., "A mechanism for increased contractile strength of human pennate muscle in response to strength training: Changes in muscle architecture," *J. Physiol.*, vol. 534, no. 2, pp. 613–623, 2001.
- [76] K. A. Witte, J. Zhang, R. W. Jackson, and S. H. Collins, "Design of two lightweight, high-bandwidth torque-controlled ankle exoskeletons," in *Proc. IEEE Int. Conf. Robot. Autom.*, 2015, pp. 1223–1228.
- [77] G. M. Bryan, P. W. Franks, S. C. Klein, R. J. Peuchen, and S. H. Collins, "A hip-knee-ankle exoskeleton emulator for studying gait assistance," *Int. J. Robot. Res.*, vol. 40, nos. 4/5, pp. 722–746, 2021.
- [78] R. D. Gregg, T. Lenzi, L. J. Hargrove, and J. W. Sensinger, "Virtual constraint control of a powered prosthetic leg: From simulation to experiments with transfemoral amputees," *IEEE Trans. Robot.*, vol. 30, no. 6, pp. 1455–1471, Dec. 2014.
- [79] Y. Marinakis and M. Marinaki, "A hybrid genetic–particle swarm optimization algorithm for the vehicle routing problem," *Expert Syst. Appl.*, vol. 37, no. 2, pp. 1446–1455, 2010.
- [80] F. L. Lewis, R. Selmic, and J. Campos, Neuro-Fuzzy Control of Industrial Systems With Actuator Nonlinearities. Philadelphia, PA, USA: SIAM, 2002



Qiang Zhang (Member, IEEE) received the B.Sc. degree in mechanical engineering and the M.Sc. degree in mechanical engineering from Wuhan University, Wuhan, China, in 2014 and 2017, respectively, the M.Sc. degree in mechanical engineering from the University of Pittsburgh, Pittsburgh, PA, USA, in 2019, and the Ph.D. degree in biomedical engineering from the University of North Carolina at Chapel Hill (UNC), Chapel Hill, NC, USA, and North Carolina State University (NCSU), Raleigh, NC, in 2021.

He is currently an Advanced Rehabilitation Re-

search and Training Postdoctoral Research Fellow in the Closed Loop Engineering for Advanced Rehabilitation with the Joint Department of Biomedical Engineering, UNC/NCSU. His current research interests include biological-signal-based neuromusculoskeletal modeling, human motion intent detection, Lyapunov-based nonlinear control/adaptive control, machine-learning-based control, surface electromyography/ultrasound imaging processing, and their applications to wearable robotic devices' control and next-generation healthcare.

Dr. Zhang was a recipient of a number of awards, including the finalist for the Best Student Paper Award of the 2019 IEEE/RAS-EMBS International Conference on Rehabilitation Robotics, the 2021 UNC/NCSU BME Department Ph.D. Student Research Award, and the 2022 ASME DSCD Rising Star Award.



Krysten Lambeth (Graduate Student Member, IEEE) received the B.Sc. degree in mathematics from Salem College, Winston-Salem, NC, USA, in 2019. She is currently working toward the Ph.D. degree with the Joint Department of Biomedical Engineering, North Carolina State University, Raleigh, NC, USA, and the University of North Carolina at Chapel Hill, Chapel Hill, NC.

Her research interests include optimal and bioinspired control of rehabilitation robotics.



**Xuefeng Bao** (Member, IEEE) received the B.Sc. degree in physics from Xi'an Jiaotong University, Xi'an, China, in 2010, and the Ph.D. degree in mechanical engineering from the University of Pittsburgh, Pittsburgh, PA, USA, in 2019.

He completed his postdoctoral research with Case Western Reserve University's School of Medicine and the Advanced Platform Technology Center, a U.S. Department of Veterans Affairs Rehabilitation Research Center. He is currently a Visiting Assistant Professor with the Department of Biomedical

Engineering, University of Wisconsin–Milwaukee, Milwaukee, WI, USA. His research interests include medical robotics, human motion control, and biosignal processing.



Ziyue Sun received the B.Sc. and M.Sc. degree in mechanical engineering from University of Pittsburgh, Pittsburgh, PA, USA, in 2014 and 2017, respectively, and the Ph.D. degree in biomedical engineering from the University of North Carolina at Chapel Hill (UNC), Chapel Hill, NC, USA and North Carolina State University (NCSU), Raleigh, NC, USA, in 2022.

He is currently working with DiDi Labs, Mountain View, CA, USA, where he is developing cutting-edge algorithms for the autonomous vehicle.



**Albert Dodson** received the B.S. degree in mechanical and aerospace engineering from Cornell University, Ithaca, NY, USA, in 2010.

Before enrolling at the University of Pittsburgh, Pittsburgh, PA, USA, he worked in Industry as a Mechanical Engineer for a company that designs flight simulators for commercial and military applications. He is currently a Lab Manager with the Professor Sharma's Neuromuscular Control and Robotics Laboratory, North Carolina State University (NCSU), Raleigh, NC, USA. He is also a Research Engineer

with the Neuromuscular Rehabilitation Engineering Laboratory, NCSU. His contributions included embedded systems design for a novel robotic prosthetic leg and mechatronics design for upper limb prosthetics. His research interests include advancing the mechatronics and controls design for the exoskeleton project and designing a new ankle exoskeleton for full speed walking.



Nitin Sharma (Senior Member, IEEE) received the B.E. degree in industrial engineering from the Thapar Institute of Engineering and Technology, Patiala, India, in 2004, and the M.S. and Ph.D. degrees in mechanical engineering from the Department of Mechanical and Aerospace Engineering, University of Florida, Gainesville, FL, USA, in 2008 and 2010, respectively.

He was an Alberta Innovates-Health Solutions Postdoctoral Fellow with the Department of Physiology, University of Alberta, Edmonton, AB, Canada.

From 2012 to 2017, he was an Assistant Professor with the Department of Mechanical Engineering and Materials Science, University of Pittsburgh, Pittsburgh, PA, USA, and became an Associate Professor in 2018. Since 2019, he has been with the Joint Department of Biomedical Engineering, North Carolina State University, Raleigh, NC, USA, and the University of North Carolina at Chapel Hill, Chapel Hill, NC, USA.

Dr. Sharma has received the O. Hugo Schuck Award for the Best Application Paper from the 2008 American Control Conference. His research in hybrid exoskeletons is funded by National Science Foundation (NSF) awards and National Institutes of Health. He also received the NSF CAREER Award in 2018, the IEEE Control Systems Technology Award in 2019, and the NIBIB Trailblazer Award in 2021.